Geochemistry, Geophysics, Geosystems

RESEARCH ARTICLE
10.1029/2019GC008882

Special Section:
Carbon degassing through volcanoes and active tectonic regions

Linking Subsurface to Surface Using Gas Emission and Melt Inclusion Data at Mount Cleveland Volcano, Alaska

C. Werner[1,2], D. J. Rasmussen[3,4], T. Plank[3], P. J. Kelly[1], C. Kern[1], T. Lopez[5], J. Gliss[6], J. A. Power[7], D. C. Roman[8], P. Izbekov[5], and J. Lyons[7]

[1]U.S. Geological Survey Cascades Volcano Observatory, Vancouver, WA, USA, [2]U.S. Geological Survey (Contractor), New Plymouth, New Zealand, [3]Lamont-Doherty Earth Observatory, Columbia University, New York, NY, USA, [4]National Museum of Natural History, Smithsonian Institution, Washington, DC, USA, [5]Alaska Volcano Observatory, Geophysical Institute, University of Alaska Fairbanks, Fairbanks, AK, USA, [6]Norwegian Meteorological Institute, Oslo, Norway, [7]U.S. Geological Survey Alaska Volcano Observatory, Anchorage, AK, USA, [8]Earth and Planets Laboratory, Carnegie Institution for Science, Washington, DC, USA

Key Points:
- Mount Cleveland volcano emitted up to 324 t/day SO_2 in July 2016 and its gas plume had a molar H_2O/SO_2 ratio of 600 ± 53
- Melt inclusions were used to derive an empirical degassing model, which can explain the gas composition by degassing a conduit from 0.5–3 km
- The total volume of magma estimated to degas each year is between 5 and 9.8 Mm^3, and the ratio of intrusive to extrusive magma is 13:1

Supporting Information:
- Supporting Information S1
- Tables S1-S6

Correspondence to:
C. Werner,
cwerner@volcanogeochemistry.com

Citation:
Werner, C., Rasmussen, D. J., Plank, T., Kelly, P. J., Kern, C., Lopez, T., et al. (2020). Linking subsurface to surface using gas emission and melt inclusion data at Mount Cleveland volcano, Alaska. *Geochemistry, Geophysics, Geosystems*, *125*, e2019GC008882. https://doi.org/10.1029/2019GC008882

Received 31 DEC 2019
Accepted 9 APR 2020
Accepted article online 21 MAY 2020

Abstract Mount Cleveland is one of Alaska's most active volcanoes, yet little is known about the magmatic system driving persistent and dynamic volcanic activity. Volcanic gas and melt inclusion (MI) data from 2016 were combined to investigate shallow magmatic processes. SO_2 emission rates were between 166 and 324 t/day and the H_2O/SO_2 was 600 ± 53, whereas CO_2 and H_2S were below detection. Olivine-, clinopyroxene-, and plagioclase-hosted MIs have up to 3.8 wt.% H_2O, 514 ppm CO_2, and 2,320 ppm S. Equilibration depths, based on MI H_2O contents, suggest that a magmatic column extended from 0.5 to 3.0 km (~10–60 MPa). We used MI data to empirically model open-system H-C-S degassing from 0 to 12 km and found that a column of magma between 0.5 and 3 km could produce the measured gas H_2O/SO_2 ratio. However, additional magma deeper than 3 km is required to sustain emissions over periods greater than days to weeks, if the observed vent dimension is a valid proxy for the conduit. Assuming an initial S content of 2,320 ppm, the total magma supply needed to sustain the annual SO_2 flux was 5 to 9.8 Mm^3/yr, suggesting a maximum intrusive-to-extrusive ratio of 13:1. The model predicts degassing of <50 t/day CO_2 for July 2016, which corresponds to a maximum predicted CO_2/SO_2 of 0.2. Ultimately, frequent recharge from deeper, less degassed magma is required to drive the continuous activity observed over multiple years. During periods of recharge we would expect lower H_2O/SO_2 and measurable volcanic CO_2.

1. Introduction

Connecting surface observations at volcanoes with ongoing subsurface magmatic processes is a prerequisite to improve eruption forecasts. Study of the rates and composition of gas emissions and petrologic analysis, including assessment of volatile contents in melt inclusions, are key for understanding the behavior of magmatic systems, but only rarely are they paired (Aiuppa et al., 2010; Burton et al., 2007; Shinoara et al., 2003). Magmatic volatile contents and degassing behavior fundamentally control the physical properties of magma and thus the eruptive behavior of volcanoes (Cashman, 2004). Melt inclusion volatile contents can shed light on these subsurface degassing processes and should be relatable to gas emissions and compositions measured at the surface (Métrich & Wallace, 2008). Likewise, gas emission rates and composition measured at the surface may give real-time information on the degassing behavior of the magma (Aiuppa et al., 2010; Allard et al., 2016; Fischer et al., 1996; Hidalgo et al., 2018; Werner et al., 2011, 2013), but these data alone are oftentimes insufficient to understand the depth or nature of ongoing processes. Therefore, combining these two types of data is a very powerful approach for probing the magmatic processes of a particular system (Aiuppa et al., 2010; Burton et al., 2007; Shinoara et al., 2003).

Multicomponent Gas Analyzer System (MultiGAS) instruments (Aiuppa et al., 2005; Shinohara, 2005) have vastly improved our understanding of degassing behavior and chemical trends, particularly at open-system volcanoes (Aiuppa et al., 2017; Allard, Aiuppa, et al., 2016), where often no accessible fumaroles exist. Such measurements can include the assessment of magmatic H_2O at active, open-vent volcanoes, unlocking great potential to probe the inner workings of these magmatic systems (Aiuppa et al., 2010; Allard et al., 2016).

Alongside developments in gas chemistry measurements, technological advancements in measuring SO_2 emissions, including SO_2 cameras (Bluth et al., 2007; Mori & Burton, 2006) are allowing for higher-rate time series of SO_2 emission data to be collected (Pering et al., 2016; Tamburello et al., 2013).

Concurrent with advances in gas measurements are improvements in our ability to extract accurate records of magma degassing paths from melt inclusions (Métrich & Wallace, 2008). Melt inclusions record magmatic differentiation processes, including crystallization, mixing, and, most importantly, degassing (Danyushevsky et al., 2002; Lowenstern, 1995), but working with melt inclusions can be challenging. The largest issue is the loss of CO_2 to vapor bubbles (Hartley et al., 2014; Moore et al., 2015). However, effective solutions to such postentrapment modifications exist (Danyushevsky & Plechov, 2011; Lloyd et al., 2013; Mironov et al., 2015; Rasmussen et al., in press). Therefore, melt inclusions can provide important context for the interpretation of gas data. The solubility of a mixed H_2O-CO_2 vapor in melt is largely dependent on pressure, with weaker dependencies on temperature, composition, and possibly fO_2 (Moore, 2008). This understanding has led to robust models for degassing of magmatic H_2O and CO_2 that have good agreement with available experimental data (Iacono-Marziano et al., 2012; Newman & Lowenstern, 2002; Papale et al., 2006). Conversely, saturation of S-bearing phases and partitioning of S into a vapor phase are complex processes that are critically dependent on the evolving oxidation state of the magma, in addition to pressure, temperature, and melt composition (Fiege et al., 2015). Models to predict S degassing exist, yet provide conflicting results (Burgisser et al., 2015; Moretti & Papale, 2004; Witham et al., 2012), and thus the capacity of such generalized models for accurately reconciling measured gas compositions at the surface and melt inclusion observations of the subsurface is unclear. This is a major shortcoming given that S is the most commonly measured gas because it can be sensed remotely; indeed, for many volcanoes, it is the only measured volcanic gas species that is routinely measured from space (Carn et al., 2017).

Here we combine observations of gas emissions and melt inclusions at Mount Cleveland volcano, Alaska (Figure 1), one of the most active and remote volcanoes in the Aleutians. Our goal is to develop a framework for understanding magmatic processes at depth using gas observations at the surface and melt inclusions in eruptive products to understand the plumbing system of Cleveland volcano. We report gas measurements from Mount Cleveland collected in July 2016, which was during a period of passive degassing ~3 months after the last period of dome growth and explosions (April–May 2016). We investigate melt inclusions from several Holocene tephra samples, focusing on a bomb that erupted in May 2016. A fundamental assumption of this work is that the magmatic system that produced the studied bomb was the same as the system that produced the measured gas emissions, which we suggest is reasonable given their temporal proximity. Melt inclusions are inferred to have been entrapped over a range of depths and span the complete compositional spectrum observed at Cleveland (basalt-dacite). To explain the gas emission rate and composition data, we develop an empirical mass balance degassing model for H_2O-CO_2-S using melt inclusion data. We show that the H_2O/SO_2 of the vapor (~600, molar) is most consistent with degassing of magma within a shallow conduit (~0.5–3.0 km, below the summit), which leads to an exploration of the physical aspects of the conduit system required to explain the observed level of SO_2 emissions. We compare the overall magma budget required to sustain the long-term SO_2 flux and compare this with previous magma budgets derived from satellite-measured heat output, and predict intrusive-extrusive ratios from these data.

2. Background

Mount Cleveland volcano (52.825°N, 169.944°W, 1,730 m summit elevation) is an andesitic stratovolcano and one of the most active volcanoes in the United States (Figure 1), with eruptive activity detected every year since 2005 (Cameron et al., 2017; Dixon et al., 2015; Dixon et al., 2017; Herrick et al., 2014). Much of what we know about the eruptive and long-term behavior of Mount Cleveland comes from satellite data (Dean et al., 2004; Wang et al., 2015; Werner et al., 2017) and infrasound monitoring (De Angelis et al., 2012). Descriptions of ongoing activity is also given in the Alaska Volcano Observatory's annual reports (Cameron et al., 2017; Dixon et al., 2015; Herrick et al., 2014; Neal et al., 2011). Phases of dome growth, lava drain back, and explosions are intermittent, while heat and gas flux are persistent (Werner et al., 2017). Between 2011 and 2015, Werner et al. (2017) documented 32 explosions and 11 periods of dome growth. The magnitude

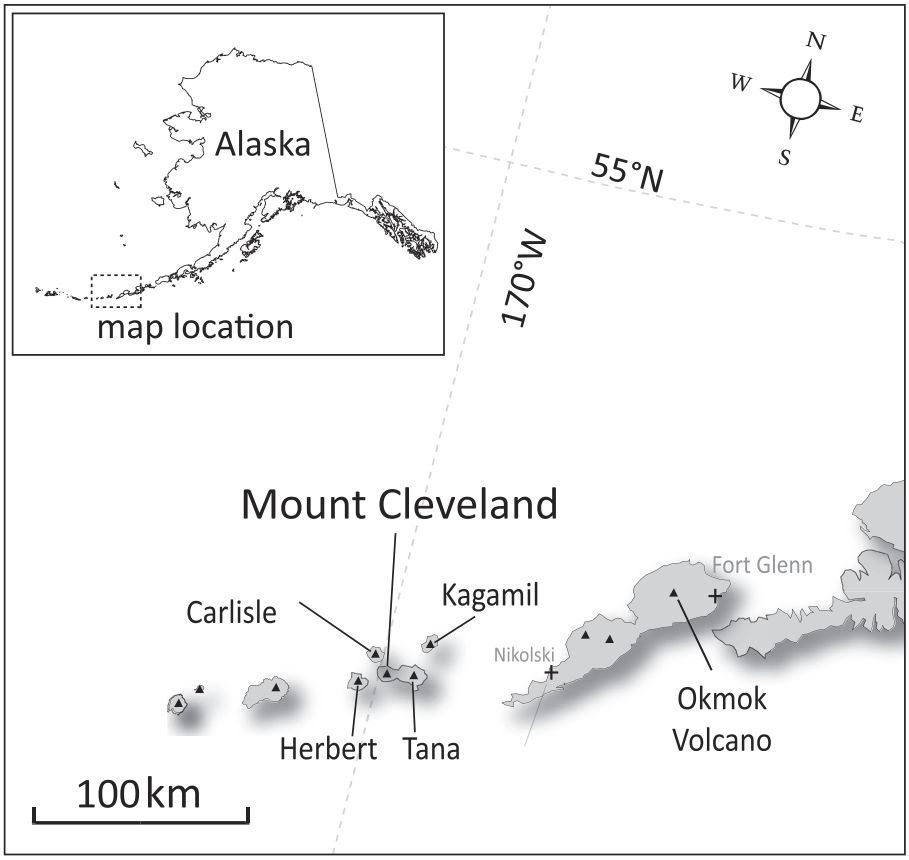

Figure 1. Location of Mount Cleveland volcano, ~70 km west of the settlement of Nikolski, Alaska, in the Central Aleutian arc. Volcanoes are shown with triangles and settlements with plus symbols.

of lava extrusion is small, as is discussed below. Mount Cleveland exhibits both flat "pancake" and axisymmetric morphology of the domes and observations of lava drain back between periods of dome growth, which suggest that the shallow magma has a low viscosity (Fink & Griffiths, 1998). Emplaced domes are more often removed by small explosions than through drain back, but both types of behavior leave an open vent in the central crater region, sometimes in the center of the previously emplaced dome. Estimates of the vent radii range from 5 to 23 m as determined from multiple observations of satellite imagery (Werner et al., 2017) and was 15 m in July 2016.

SO_2 emission rates were measured for the first time in 2015 during a heightened period of activity including dome growth (Werner et al., 2017). Emissions varied between 400 and 860 t/day SO_2 over a period of 5 days in August 2015 when CO_2/SO_2 ratios were <3, indicative of shallow magma degassing. The average rate of lava extrusion between 2011 and 2015 was 0.28 $m^3\ s^{-1}$ calculated for nine periods of rapid increase in thermal output associated with dome growth, where each episode lasted <5 weeks (Werner et al., 2017). The rates observed during individual periods of dome growth at Mount Cleveland are similar to those observed at volcanoes like Merapi (Siswowidjoyo et al., 1995), and long-term rates observed at Popocatepetl (Gómez-Vazquez et al., 2016; Ogburn et al., 2015; Werner et al., 2017). The total extruded volume was between 1.9 and 5.8 Mm^3 from 2011 to 2015, which again is similar to Merapi (≤8 Mm^3 in <5 years, Siswowidjoyo et al., 1995), but low compared to dome growth observed at more silicic volcanoes like Redoubt volcano in Alaska (e.g., 72 Mm^3 from 2009 eruption, Bull & Buurman, 2013). During the 2015 dome growth event, the extruded volume was between 0.24 and 0.73 Mm^3. Werner et al. (2017) suggested such events can only account for roughly half of the long-term thermal budget, requiring additional unerupted, near-surface magma to account for the remaining heat flux. The same study suggested that maintaining the long-term heat flux and degassing likely requires convection of magma to shallow levels in the conduit.

In the months preceding the observations in July 2016, Mount Cleveland experienced three small explosions recorded between 16 April and 10 May, followed shortly thereafter by an extrusion of a lava dome between 17 and 20 May. This dome was similar in shape and size to multiple other domes emplaced between 2011 and 2015 (Alaska Volcano Observatory unpublished data: https://avo.alaska.edu/volcanoes/activity.php?volcname=Cleveland&page=basic&eruptionid=1161). A 46-m diameter dome was present with an open central vent when observed in July 2016.

3. Methods

3.1. Airborne Volcanic Gas Measurements

The airborne measurements included gas concentrations measured using a MultiGAS system that was mounted in a Bell 407 helicopter and SO_2 column concentrations made using an upward looking miniature DOAS (Differential Optical Absorption Spectroscopy, Platt & Stutz, 2008) spectrometer system. The MultiGAS measured in situ gas compositions (H_2O, CO_2, SO_2, H_2S) at 1 Hz and included a nondispersive infrared CO_2 and H_2O analyzer (LI-COR, Inc. LI-840A, 0–5,000 ppm for CO_2, 0–80 parts per thousand for H_2O), electrochemical SO_2 (City Technology, Ltd., 2T3STF, 0–100 ppm), and H_2S sensors (City Technology, Ltd., EZT3H, 0–100 ppm) and a GPS receiver. Sensor calibrations were checked in the field with both high (SO_2 = 26 ppm, CO_2 = 2,970 ppm, H_2S = 25 ppm) and low (SO_2 = 2.1, CO_2 = 2,920 ppm, H_2S = 2.0 ppm) gas standards and CO_2 free air, and all instruments performed accurately within ±7% of the standards. The H_2S sensor's average cross-sensitivity to SO_2 was 17% and the functional lower detection limit for H_2S was estimated to be 0.4 ppmv for a 2-sigma detection above background. In addition, a temperature and relative humidity (T/RH) sensor (Vaisala HMP-60) was mounted outside the helicopter to directly measure ambient T/RH. All MultiGAS data were displayed in real time with a tablet. Further details of this airborne MultiGAS setup have been discussed previously in Werner et al. (2017). The DOAS instrument consisted of an upward looking telescope, an Ocean Optics USB2000+ spectrometer, a GPS receiver, and a BeagleBone Black embedded miniature computer for data acquisition. The instrument measured the spectral radiance of scattered solar UV radiation between 285 and 430 nm at a resolution of 0.8 nm, and spectra were recorded at 1 Hz.

A dedicated gas flight was performed on 25 July 2016 to collect in situ gas concentrations in the volcanic plume and to perform DOAS traverses beneath the plume for SO_2 emission rate determination (Figure 2). Six DOAS traverses were made downwind of the volcano, three at 2–3 km downwind and three at ~1 km downwind between 15:07 and 16:02 local time. In situ data were collected at 3 km downwind of the volcano, but as these readings were dilute (Figure 3b, plume passes 1–3), we moved closer in order to collect measurements in the more concentrated plume. In situ data were then collected 1 km downwind of the summit at altitudes between 1,650 and 1,800 m above sea level (ASL) (Figure 3b, passes 5–8). One pass intersected the plume at about 500 m downwind of the vent region (Figure 3b, pass 4). The entire flight covered an altitude range of sea level (0 m) up to 1,950 m ASL.

The spectra measured by the DOAS system were downloaded to a laptop computer and analyzed using the DOASIS software (Kraus, 2006). A standard DOAS retrieval (Platt & Stutz, 2008) was used to derive the vertical SO_2 column density above the helicopter from each recorded spectrum. First, each measurement spectrum was corrected for electronic offset and charge-coupled device (CCD) dark current, and a first-order stray light correction was performed by subtracting any baseline intensity remaining below 290 nm. Each spectrum was then divided by a clear sky reference and its logarithm was taken to obtain the optical depth. Next, the absorption cross sections of SO_2 and ozone (Bogumil et al., 2003; Vandaele et al., 2009) were fitted to the optical depth in the 310 to 325 nm wavelength region. A Ring correction spectrum was included in the fit to account for variability in the contribution of inelastic scattering to each measured radiance (Grainger & Ring, 1962). A third-order polynomial was used to account for broadband variations between the measurement and clear sky spectrum, which mostly stem from aerosol scattering and absorption. Finally, a first-order correction for slight changes in the spectrometer's wavelength calibration was included in the fit following Beirle et al. (2013).

To derive emission rates (Table 1), the vertically oriented SO_2 column densities obtained along each individual traverse were integrated, yielding SO_2 burdens in a cross section of the volcanic plume. Correction for

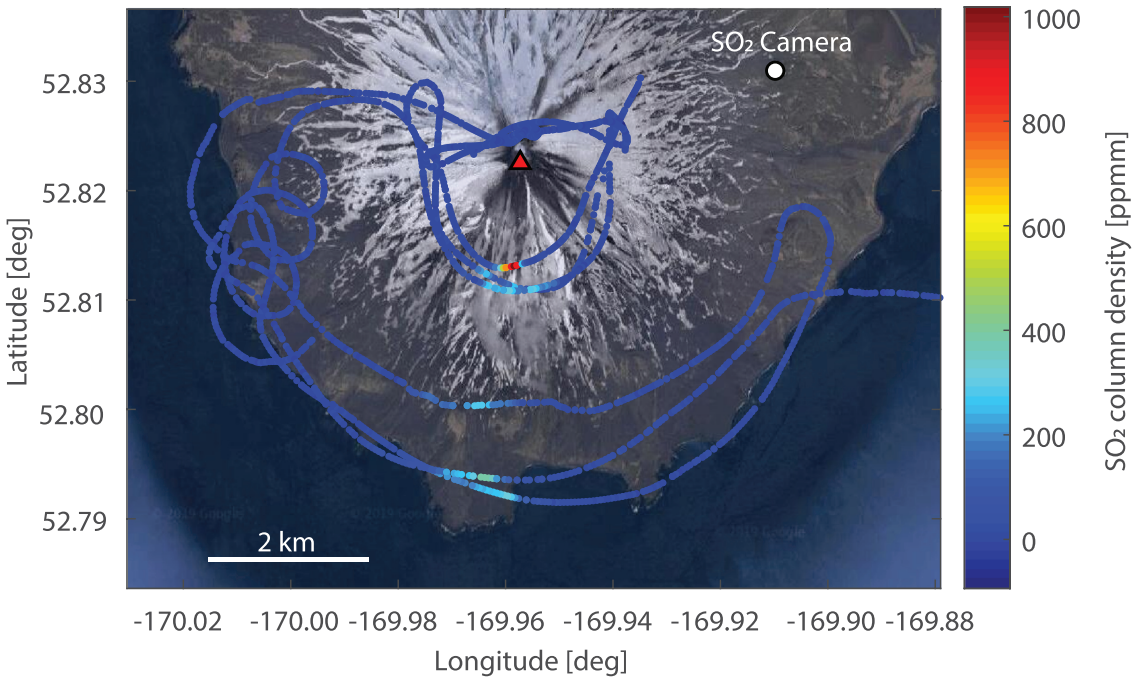

Figure 2. Google-Earth map of the southern edge of Mount Cleveland showing the location of the flight transects with the plume traversing to the south on 25 July 2016. Lighter blue and warm colors show the regions in which the SO_2 column was measured overhead by DOAS. The location of ground-based measurements (including SO_2 camera) on 24 July 2016 is shown when the plume was traversing to the east-southeast.

nonperpendicular transects to the wind direction were made as needed, and then these burdens were multiplied by the plume speed to obtain emission rates. This spatial analysis was performed using MATLAB.

A plume speed of 5.8 ± 0.6 m/s was measured using the "wind circle" technique (Doukas, 2002). Both plume speed and direction can be derived by fitting a sine curve to the plot of airspeed versus flight direction. Once the best fit is obtained, the amplitude of the sine curve yields plume speed while the phase yields plume direction. The fit error yields the uncertainty of the measurement.

3.2. Thermal Infrared Imaging

Thermal images of the summit area were captured on 26 July 2016 during helicopter flights using a FLIR® Systems model SC620 camera with a 640 × 480 image size. The average air temperature was 8°C during the flight and the slant distance between the vent and camera was ~1 km. Temperatures were calculated from the thermal images after applying an atmospheric correction and using an emissivity of 0.95. Maximum pixel temperatures of 650°C were recorded around the center of the vent where degassing was focused. Temperatures on the exterior of the dome, and away from active degassing, were as low as 20°C indicating that vent was the dominant heat source.

3.3. Ground-Based SO_2 Emission Rate Measurements

On 23 and 24 July, a SO_2 camera (Kern et al., 2015) was deployed to measure continuous SO_2 emission rates on the NE-E flank of Cleveland (Figure 2). Reliable estimates of SO_2 emission rates were only possible on 24 July (thick clouds obscured our view of the volcano's summit on 23 July), when steady northerly winds carried the plume toward the southeast. Measurements were made 3.4 km east of the volcano summit, and 320 m ASL, between 18:00 and 22:15 UTC (9:00 to 13:15 local time). Starting at 19:30, the wind speed reduced, causing the plume to accumulate around the volcano summit such that the plume velocity could no longer be retrieved reliably due to different overlapping plume parcels moving in opposite directions. Therefore, our analyses were restricted to the 18:00–19:30 (UTC) time window.

The SO_2 camera system contained two UV-sensitive CCD cameras (JAI CM-140GE-UV) and a moderate resolution UV spectrometer (Ocean Optics USB2000+). Band-pass filters with transmittance windows

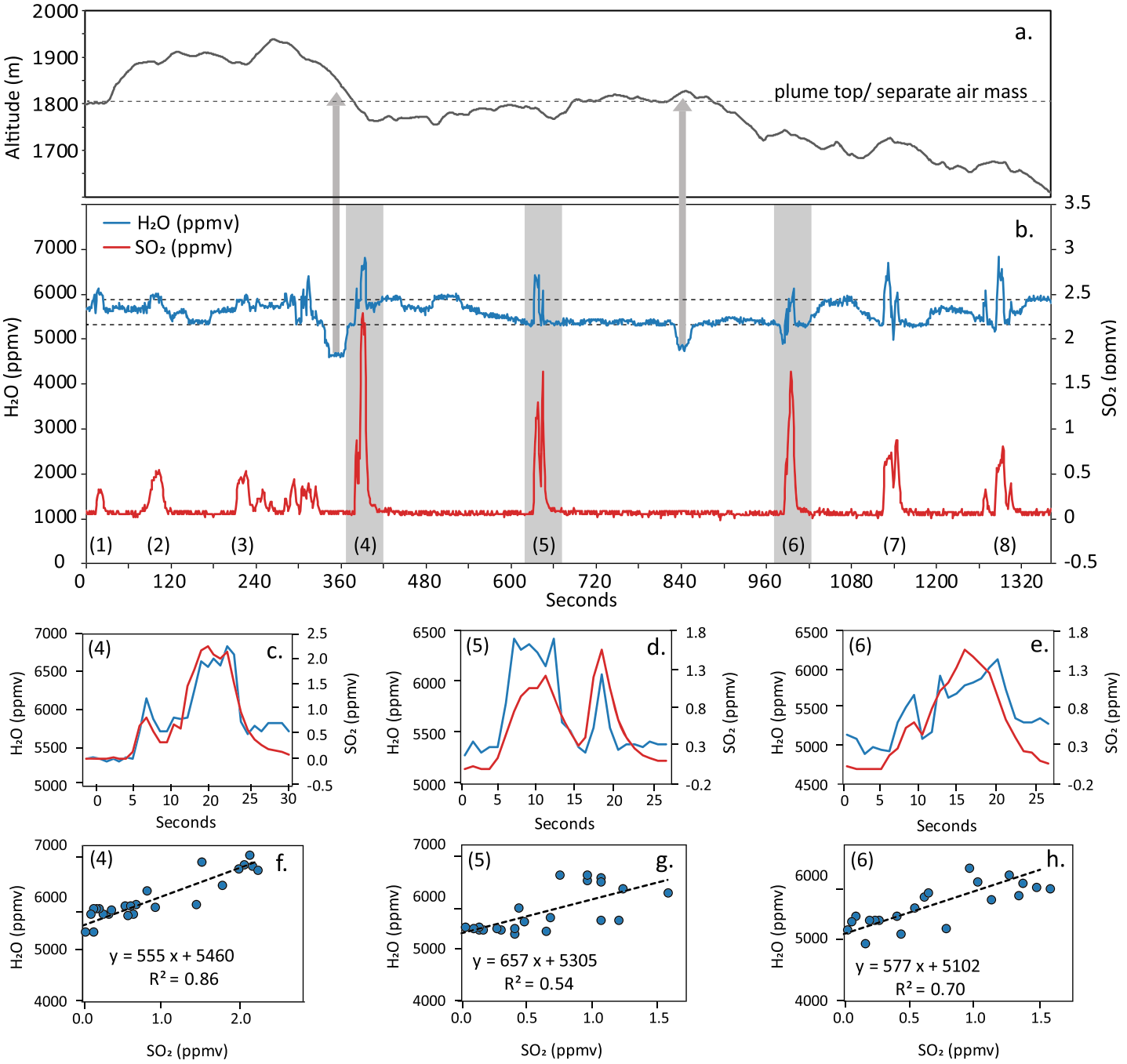

Figure 3. Plume transects and ratios determined from the airborne MultiGAS measurements. (a) Flight altitude, (b) H_2O and SO_2 concentrations in the air with time, where the peaks indicate the airborne measurement across the downwind plume and the numbers below the peaks indicate the passes through the plume (i.e., transects), (c–e) zoomed-in portions of plume concentrations shown in (b) for transects 4–6, and (f–h) H_2O versus SO_2 scatter plots resulting from plume transects 4–6.

centered at 313 and 330 nm (each with 10 nm full-width half maximum) were positioned between the camera's object lenses and detectors. Thus, imagery collected at 313 nm was sensitive to SO_2 absorption, whereas imagery collected at 330 nm was used as a reference for the background radiance, as described in previous studies (Bluth et al., 2007; Kern et al., 2010; Mori & Burton, 2006). The

Table 1
Gas Emissions Determined From Airborne Traverse Measurements

Altitude	Distance	SO_2 emission rates				CO_2 emission[a]	H_2O emission
(m)	(m)	(kg/s)	error	(t/day)	error	(t/day)	(t/day)
768	3,112	4.52	0.97	390	83	54	60,877
993	3,064	4.55	1.01	393	88	54	61,345
1,239	2,340	3.38	0.98	292	84	40	45,579
1,599	768	3.18	0.57	275	49	38	42,926
1,679	696	3.13	0.59	270	51	37	42,145
355	3,710	3.77	0.92	326	80	45	50,887
	ave	3.8		324		45	50,626
	stdev	0.6		55		7.6	8,680

[a]Assuming a C/S ratio of 0.2, see text.

spectrometer measured the incident spectral radiance in a 0.3° field of view in the center of the camera images between 285 and 430 nm. Additional details of the utilized camera system are given by (Kern et al., 2015).

The imagery collected by SO_2 camera was analyzed using the Pyplis software package (Gliß et al., 2017). Coincident on- and off-band camera images were first divided by background images collected away from the plume, then the logarithm was taken to obtain two optical depth images. In the next step, the apparent absorbance was calculated by subtracting the off-band optical depth from the on-band optical depth. The apparent absorbance was then normalized by the average radiance recorded in a small region just north of the volcano summit. In our analyses, we accounted for "light dilution," or light scattering into the instrument field of view without having passed through the plume (Kern et al., 2010), using the image-based method described by Campion et al. (2015). The analysis yielded an atmospheric scattering coefficient of 0.137 km^{-1} at 313 nm, indicating ~1/3 of the measured radiation at this wavelength was scattered between the plume and the instrument.

SO_2 column densities were retrieved from the spectra recorded by the integrated DOAS spectrometer between 310 and 330 nm (wavelengths chosen to be consistent with camera filter wavelengths) using a standard retrieval as described above (Platt & Stutz, 2008). The optical depth images were then calibrated and converted to SO_2 column density images (Figure A1.) by comparing the DOAS column densities to the measured plume optical densities in the DOAS field of view within the images and deriving a linear relationship. The plume velocity was determined at each pixel using a hybrid optical flow method that includes a correction for ill-constrained plume tracking in the often-homogeneous plume center (Gliß et al., 2018). Finally, the SO_2 emission rate was determined by multiplying the column density with the orthogonal plume velocity and integrating along a cross section of the gas plume near the volcano's vent (see Figure A1).

3.4. Petrological Analysis

We analyzed the major-element compositions and volatile contents (H_2O, CO_2, S, Cl) of 22 melt inclusions hosted in olivine, clinopyroxene, and plagioclase crystals and two matrix glasses from tephras that erupted from Mount Cleveland (Table S1). Most of the melt inclusions ($n = 15$) and matrix glasses were recovered from the outer 2 cm of a <10 cm volcanic bomb that erupted in May 2016 (except one melt inclusion that is from the bomb interior). These melt inclusions are hosted in olivine ($n = 2$), clinopyroxene ($n = 8$), and plagioclase feldspar ($n = 5$). These melt inclusions are used to examine magma depth in the modern plumbing system. The other studied melt inclusions ($n = 7$) are hosted in loose olivine found in tephra samples and are from two more mafic samples. One is ash and lapilli deposited on top of a lava talus slope on the west flank of the volcano (CL15PS06); this likely includes material from the recent eruptive history of Cleveland. The other (CV15DJR09E) is a weathered, dark ash layer in an extensive Holocene tephra section on the east flank of the volcano described by Neal et al. (2015). All melt inclusions plot along the same major-major and major-volatile element trends (Figure A2). Therefore, the Holocene melt inclusions were used with the 2016 melt inclusions to examine the chemical evolution of the system and model the degassing path. H_2O and CO_2 contents of melt inclusions were measured using a Thermo-Nicolet Nexus 670 Fourier transform infrared spectrometer coupled with a Continuum IR microscope at the American Museum of Natural History (AMNH). Analyses followed established procedures (e.g., Rasmussen et al., 2018). Major element and volatile (S, Cl) contents of melt inclusions and major element contents of host minerals were analyzed using a Cameca SX-100 electron microprobe at the AMNH over four sessions. Glass 892-1 and San Carlos olivine were used as check standards (Table S2). Results were typically within 5% of accepted values, except for P (described in the supporting information) and S. S concentrations were 70–75% of accepted values, which is likely an effect of measuring off peak (e.g., Lloyd et al., 2010; Zimmer et al., 2010). We adjusted the S contents of sample analyses by the offset measured in standard basaltic glasses (e.g., Rasmussen et al., in press). This correction has a negligible effect on the salient aspects of the degassing

modeling (i.e., H_2O/SO_2 and S flux) because the correction factor was similar for all melt inclusions. We also report new major element analyses, collected via Inductively Coupled Plasma Emission Spectrometry at Lamont-Doherty Earth Observatory, for a range of bulk rock samples from Cleveland, including those that host the melt inclusions (Table S5), using the methods reported in Wade et al. (2005).

All melt inclusions hosted in olivine were corrected for postentrapment crystallization/melting (PEC/PEM; i.e., growth or dissolution of olivine at the olivine-melt interface) and vapor bubble growth (i.e., formation of a vapor bubble after entrapment containing a CO_2-rich vapor) using MIMiC (Rasmussen et al., in press). Only the PEC/PEM-and bubble-corrected compositions are discussed in this paper. Uncorrected data are presented in Table S4. Melt inclusions in plagioclase and pyroxene hosts were not corrected for PEC/PEM. These samples do not appear as outliers on major element plots (e.g., Figure A2a), indicating that it is unlikely that PEC/PEM had a significant influence on melt composition. These melt inclusions were also not corrected for bubble growth because the CO_2 contents of the glass were below detection limits (for both CO_3^{2-} and CO_2), implying the CO_2 content of the coexisting bubble would also be negligible. Significant exsolution of H_2O into bubbles is not expected because of the large molar volume of H_2O in a vapor phase (Steele-Macinnis et al., 2011). Melt inclusions show clear evidence of diffusive loss of H^+ (Figure A2b). We corrected for this diffusive loss by fitting a rhyolite-MELTS model of ascent, degassing, and crystallization to the highest-water-content melt inclusions along the liquid line of descent (see Rasmussen, 2019), a commonly employed approach (e.g., Lloyd et al., 2013; Rasmussen et al., 2018).

3.5. Degassing Model

Here we summarize the degassing model used in this study, which is developed further in Rasmussen (2019). The model describes the compositional evolution of melt and vapor during magma ascent, degassing, and crystallization. We took a similar approach to several earlier studies (Johnson et al., 2010; Sisson & Layne, 1993; Spilliaert et al., 2006), which involves using melt inclusion data to define the degassing path and then calculating the composition of the vapor by mass balance. The entirety of the melt inclusion data set was used to make the model because all melt inclusions have systematic major and volatile element trends. The model starts at 12-km depth, consistent with the maximum entrapment pressure of melt inclusions from the Holocene mafic samples, and degassing calculations are performed at ~0.05-km steps until a depth of 0.01 km is reached. Depth is converted to pressure using a crustal density model developed for Mount Cleveland (Figure A3). Melt H_2O and CO_2 contents at a given pressure are determined using a degassing path calculated using VolatileCalc (Newman & Lowenstern, 2002) with initial conditions reflecting those of the least degassed melt inclusion (CL06MI03): 3.8 wt% H_2O, 49 wt% SiO_2, and 1100°C, calculated using the olivine-melt thermometer (Equation 4 of Putirka et al., 2007). We use an initial CO_2 content of ~700 ppm, which is appropriate for the starting depth (12 km) of the model. We stress that the selection of starting depth (hence, starting CO_2) does not influence the shallower parts of the model (i.e., below the onset of water degassing) significantly, provided the model starts at a depth greater than that of the onset of water degassing, because degassing is modeled as occurring in an open system (see below). VolatileCalc was the selected vapor-saturation model because it is widely used for basaltic systems, not enriched in alkalis, making our results comparable with other studies. Additionally, it is one of the only solubility models available that calculates degassing paths. Degassing is modeled as open system, meaning crystals and vapor are removed from the melt at each step. This is consistent with H_2O-CO_2 trends of corrected melt inclusion compositions (e.g., high H_2O contents are observed in melt inclusions with CO_2 contents below detection limits) and the open-vent nature of Mount Cleveland (Lu & Dzurisin, 2014; Werner et al., 2017). The melt fraction at each depth step is tracked by K_2O (assumed to be incompatible in the separating vapor and crystal assemblage), which is calculated using a linear regression of the corrected H_2O and K_2O contents of melt inclusions (Figures A2d and A4a). While previous approaches assume that a fluid/melt partition coefficient governs S behavior (e.g., Sisson & Layne, 1993), here we take an empirical approach and calculate the S content of the melt at each depth step using the calculated K_2O content and a function relating S and K_2O contents determined by a least squares regression of melt inclusion data (Figures A2c and A4b). The vapor composition is calculated by mass balance, accounting for incompatible behavior of H_2O, CO_2, and S during crystallization. To assess uncertainty, we use a Monte Carlo approach in which we repeated the calculation for 200 simulations, while randomly resampling melt inclusion data over their uncertainties (1σ confidence intervals of 13%, 16%, and 4% on average for K_2O, S, and H_2O, respectively).

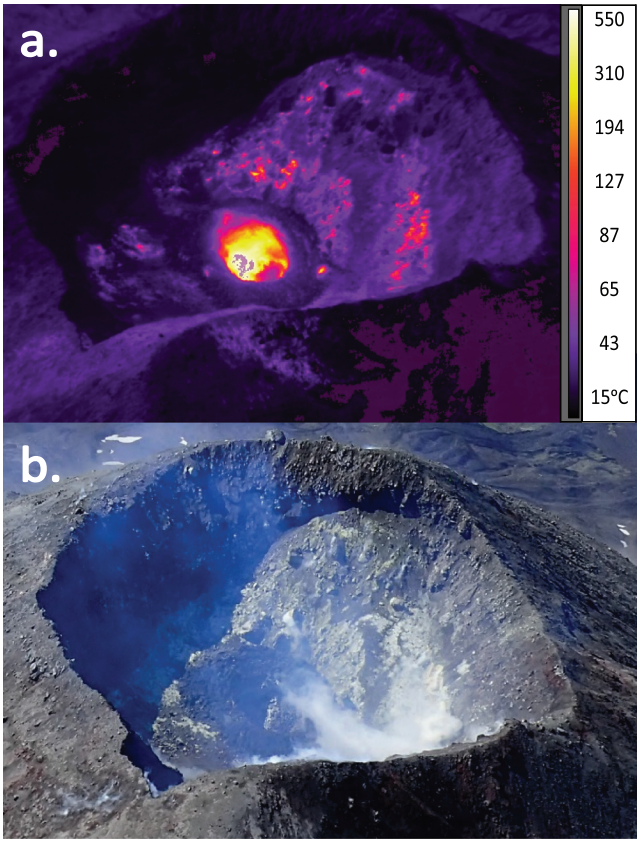

Figure 4. (a) Thermal infrared image of the vent in the central crater (85 m radius) of Mount Cleveland on 26 July 2016. The maximum temperature in this image was 650°C. (b) Visual image of the central crater on the same day. The small dome in the center of the crater had an estimated radius of 46 m and surrounded an open vent (15 m radius). The gas was observed to be superheated and streaming out of the central vent. As the gas cooled, water vapor condensed inside the crater before reevaporating downwind.

Our model includes several simplifying assumptions. First, the model is reliant on H_2O-CO_2 solubility models for basaltic compositions, whereas the Cleveland system ranges from basalt to at least dacite in melt composition. However, we stress that solubility models for melts spanning the compositional spectrum observed converge at low pressure (<100 MPa; Figure A5), which is where our study is focused. Additionally, melt inclusion data show an inverse relationship between volatile content and melt evolution. Therefore, the greatest disparity between the modeled and actual melt compositions exists at shallow depths, where the saturation models are less sensitive to melt composition. Second, K_2O is assumed to behave incompatibly. As melt evolves into dacitic compositions, MELTS models predict that K_2O partitioning into feldspar becomes significant. However, feldspars measured from the 2016 sample have very low K_2O contents (D = ~0.03–0.07; Rasmussen, 2019), suggesting that K_2O can be approximated as perfectly incompatible. Third, the modeling performed here is very sensitive to the method of regressing the melt inclusion data. We used a linear regression to describe H_2O-K_2O trends in melt inclusion data and log-linear regression to describe S-K_2O trends. Although other methods for regressing the data exist, our approach produces the best fits to the data. Finally, we assume all S in the vapor exists as SO_2. This is a simplification because other S-bearing volatile species could exist (e.g., S_2, H_2S). However, SO_2 is the only S-bearing vapor that has been detected in Cleveland gases (Werner et al., 2017), which is what one would expect at low pressures (Symonds et al., 1994).

4. Results

4.1. Airborne Measurements

Conditions during the airborne measurements were clear skies, optimal winds speeds, and low humidity. Incandescence was observed in the vent on both 25 and 26 July 2016 in the center of a previously extruded dome (Figure 4). Maximum apparent temperatures recorded with a FLIR were ~650°C, and the gas emitting from the central vent area was superheated (invisible directly above vent). Condensation of water vapor was observed above the vent, indicating rapid cooling of the gas (Figure 4), but the condensed water then reevaporated resulting in a transparent plume downwind of the volcano. Consequently, airborne measurements were made where there was no visible plume.

Vertical profiles of ambient temperature, H_2O, and CO_2 on 25 July show that the atmosphere was dry and stable during the airborne measurements, with some minor stratification and heterogeneity with respect to H_2O and CO_2 mixing ratios at altitudes from 1,650–1,900 m. The ambient CO_2 concentration increased gradually with altitude over the duration of the flight and no discernable volcanic CO_2 signal was detected over background levels and instrumental noise (±0.5 ppmv, 1σ) (Figure 5b). Ambient background H_2O away from the volcano was variable and indicated the presence of distinct air parcels separated at ~1,700; 1,825; and 1,900 m (Figure 5d). Ambient H_2O near the volcano sometimes differed from the H_2O away from the volcano (note that the base of the H_2O peak at the volcano shown in red in Figure 5d is lower than that observed away from the volcano shown in blue), but the in-plume H_2O anomalies (meaning those that were coincident with volcanic SO_2 peaks) clearly exceeded any background near the volcano (Figures 3 and 5d). Finally, small apparent H_2S peaks (up to 0.2 ppmv) were recorded during the plume-sampling. However, after correcting for cross-sensitivity of the H_2S sensor to SO_2 (16.5 ± 2.3%) all of the calculated H_2S/SO_2 ratios are well below the 1σ error estimate of the measurements (H_2S/SO_2 = ±0.048). Thus, we conclude that the

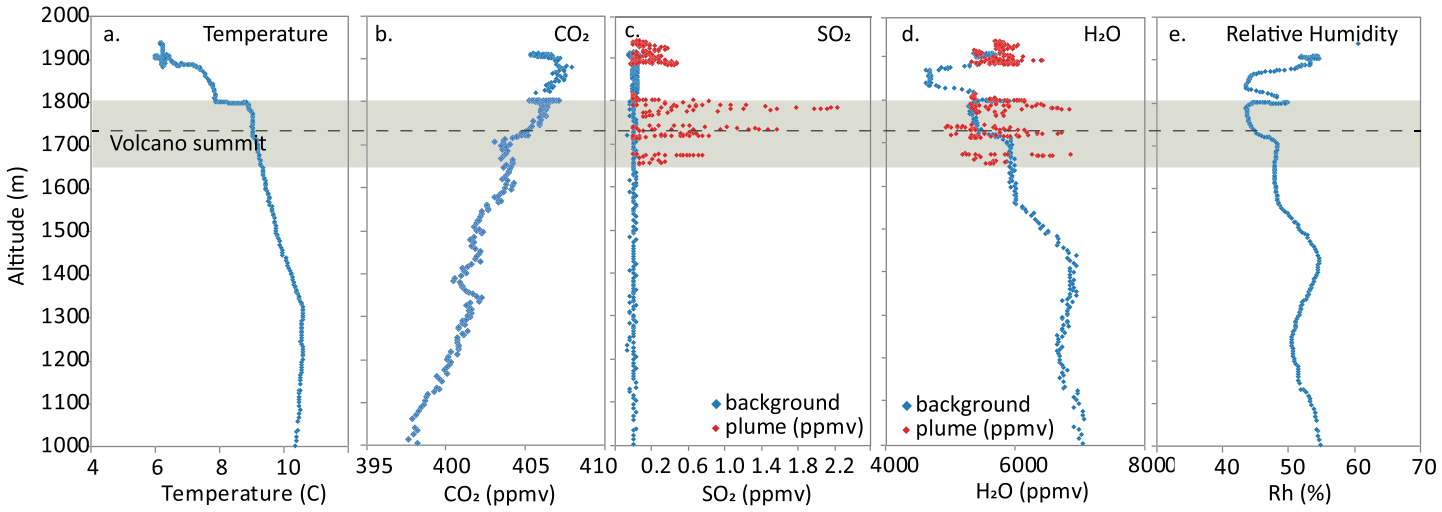

Figure 5. Vertical profiles of measured constituents collected with MultiGAS instrumentation during the airborne measurement. The blue indicates background concentrations away from the volcano, and red indicates the downwind plume component. (a) The vertical profile of temperature, (b) CO_2 mixing ratio in the air (no plume CO_2 detected), (c) SO_2 measured in background air showed no SO_2 anomalies, whereas downwind passes showed variations. The passes at 1,900 m were ~5 km from the volcano, whereas the passes between 1,600–1,800 m were closer to the volcano. (d) The H_2O concentration in the background air was variable with height at upwind locations. Strong H_2O anomalies were measured at plume height downwind of the volcano. (e) Relative humidity in the plume was less than 60% for the entire measurement period.

H_2S/SO_2 ratio in the plume was less than 0.048 and that SO_2 comprised greater than 95% of total S in the plume.

Volcanic contributions of both SO_2 and H_2O were detected downwind of the volcano at multiple altitudes between 1,650 and 1,800 m (Figure 5). As expected, SO_2 was not detected in background air (Figure 5c). Two independent sensors (one based on infrared absorption, Licor 840A; another based on capacitance, Vaisala HMP-60) were used to measure water vapor content and showed good agreement (Figures 5d and 5e). Relative humidity was <60% for the duration of the flight and 45% to 50% at plume height (Figure 5e). This corresponds to concentrations of background air ranging from 5,500 to 6,000 H_2O ppmv at the plume altitude. Maximum in-plume concentrations of 2.2 and ~1,500 ppmv (above background) were measured for SO_2 and H_2O, respectively, during Transect 4 (Figure 3) at ~1,780-m altitude and ~500 m downwind of the summit.

Our measurements of Mount Cleveland's gas composition are dominated by H_2O (99.83 mol%) with traces of SO_2 (0.17 mol%) and CO_2 below detection limits. The highest concentration SO_2 and H_2O anomalies (Figure 3b, Transects 4–6) were used to calculate the H_2O/SO_2 ratio (Figures 3c–3e), the values of which varied between 555 and 660 (Figures 3f–3h) with an average of 600 ± 53. Higher ratios were calculated for data collected further from the volcano, but these three transects are favored because they were collected closest to the vent region and showed the highest concentrations in SO_2, indicating they are the least susceptible to any possible complication that might arise from plume transport in a heterogeneous background atmosphere (e.g., Kelly et al., 2013). While we did not detect CO_2 above ambient background, we can use the detection limit of the CO_2 analyzer to define a maximum CO_2/SO_2 ratio of the volcanic gas, as was done for the measurements made in 2015 (Werner et al., 2017). If we conservatively define the CO_2 detection limit as 3 times the noise of the analyzer (i.e., $3\sigma = 1.5$ ppmv), then we can calculate a CO_2/SO_2 ratio based on the SO_2 data for which we would have observed a statistically significant anomaly. In 2015, the maximum SO_2 measured was 0.53 ppmv and the resulting CO_2/SO_2 was <3. In 2016, the maximum SO_2 measured was 2.2 ppmv, suggesting CO_2/SO_2 could not have been higher than 0.7 or it would have resulted in a statistically significant volcanic CO_2 signal above ambient background values.

Emission rates of SO_2 during the airborne measurement on 25 July 2016 ranged from 3.1 to 4.55 kg/s (270 to 390 t/day), with an average ± standard deviation of 324 ± 55 t/day (Table 1) that was higher than that of the

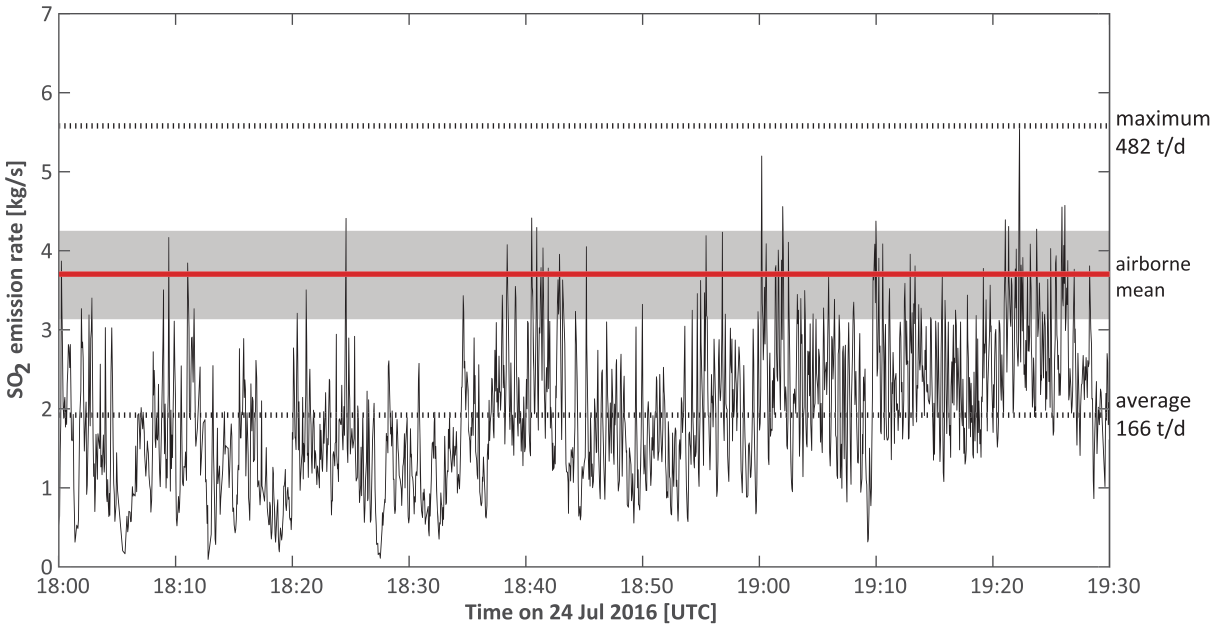

Figure 6. SO_2 fluxes measured with a UV camera on 24 July 2016. The band shows the range of airborne measurements.

ground-based measurements made on the previous day (reported below). The emission rates in 2016 are somewhat lower than measurements made in 2015 (400–860 t/day) which were made during or immediately after a period of active dome growth (Werner et al., 2017). While within error, we note that the highest SO_2 emission rates during the airborne measurement in 2016 were made from the lowest altitudes (Table 1). If a real variation, this would suggest that perhaps the higher altitude traverses may have missed a small portion of the plume, or alternatively, that emission rates were variable during the measurement period.

4.2. Ground-Based SO_2 Emission Rates

During the SO_2 camera measurements on 24 July 2016, Mount Cleveland's SO_2 emission rate was relatively constant, although a very slight increase in degassing appears to have occurred beginning at about 18:50 UTC. The mean emission rate for the 2-hr measurement window was 1.9 ± 0.9 kg/s (or 166 ± 78 t/day) SO_2 (Figure 6), where the error indicates the standard deviation. The maximum detected emission rate of 5.6 kg/s (482 t/day) was obtained at 19:22:17 UTC, and there is some overlap in the SO_2 emission rates determined by SO_2 camera and by airborne measurements from the previous day (Figure 6). Most of the measured variability occurred on very short timescales and was likely caused by the turbulent dynamics of the plume mixing into the background atmosphere near the summit of the volcano rather than changes in the degassing behavior.

4.3. Melt Inclusions

The juvenile bomb analyzed is an andesite with dacitic matrix glass containing (in order of decreasing abundance) plagioclase feldspar, clinopyroxene, and rare olivine. Most olivines have disequilibrium textures, showing some signs of partial resorption. The other Holocene samples with melt inclusions are basaltic andesite (CL15PS06) or of unknown bulk composition (CV15DJR09E) and lack clear signs of disequilibrium. Melt inclusions in all samples are naturally glassy and fully enclosed, without clear evidence of decrepitation (photomicrographs in the supporting information; morphological data in Table S4). Vapor bubbles occur in all olivine-hosted and most plagioclase-hosted melt inclusions. Clinopyroxene-hosted melt inclusions lack vapor bubbles. Crystal inclusions are absent from most (18 of 22) melt inclusions. Olivine-hosted melt inclusions in the 2016 sample have small crystals that nucleated on a crystal inclusion and/or vapor bubble, which we speculate might be olivine. None of the melt inclusions with crystal inclusions have irregular major

Geochemistry, Geophysics, Geosystems

10.1029/2019GC008882

Table 2
Melt Inclusion and Matrix Glass Data

Sample	MI host	Parent (WR) sample	SiO_2 (wt.%)	TiO_2 (wt.%)	Al_2O_3 (wt.%)	FeO^T (wt.%)	MnO (wt.%)	MgO (wt.%)	CaO (wt.%)	Na_2O (wt.%)	K_2O (wt.%)
16IPE1BextMG01	N/A	16IPE1B	64.94	1.29	14.57	7.52	0.16	1.77	4.91	4.16	1.64
16IPE1BextMG03	N/A	16IPE1B	64.97	1.25	14.98	7.24	0.15	1.52	4.99	4.38	1.65
16IPE1BintPLAGMI01	Plagioclase	16IPE1B	62.76	1.31	13.95	7.80	0.15	2.06	5.11	3.97	1.51
16IPE1BextOLVMI04	Olivine	16IPE1B	54.90	1.09	18.53	7.66	0.14	2.98	8.18	3.87	0.52
16IPE1BextOLVMI06	Olivine	16IPE1B	49.39	1.05	20.34	7.76	0.13	4.63	11.09	3.04	0.40
16IPE1BextPLAGMI02	Plagioclase	16IPE1B	68.09	0.69	14.38	4.48	0.10	0.98	3.65	4.36	2.04
16IPE1BextPLAGMI12	Plagioclase	16IPE1B	63.13	1.03	15.79	6.40	0.15	1.62	5.00	4.13	1.51
16IPE1BextPLAGMI14	Plagioclase	16IPE1B	65.35	1.21	14.22	6.95	0.14	1.41	4.33	4.46	1.69
16IPE1BextPLAGMI15B	Plagioclase	16IPE1B	61.51	1.09	15.96	6.57	0.15	1.55	4.78	4.39	1.51
16IPE1BextPXMI07A	Clinopyroxene	16IPE1B	59.52	0.92	17.65	6.10	0.12	2.47	5.74	4.31	1.54
16IPE1BextPXMI07B	Clinopyroxene	16IPE1B	61.43	1.02	16.13	6.37	0.14	1.99	5.34	4.15	1.63
16IPE1BextPXMI07C	Clinopyroxene	16IPE1B	61.64	1.07	16.39	6.16	0.13	2.11	4.97	4.22	1.61
16IPE1BextPXMI07D	Clinopyroxene	16IPE1B	60.01	1.30	15.96	6.98	0.16	2.21	5.40	3.99	1.47
16IPE1BextPXMI08	Clinopyroxene	16IPE1B	66.60	0.74	13.37	5.79	0.17	1.81	4.72	3.93	1.70
16IPE1BextPXMI09	Clinopyroxene	16IPE1B	67.49	0.96	12.10	6.12	0.14	1.35	3.94	3.62	2.19
16IPE1BextPXMI10	Clinopyroxene	16IPE1B	62.02	1.11	15.53	7.07	0.15	1.88	4.98	4.17	1.49
16IPE1BextPXMI16A	Clinopyroxene	16IPE1B	64.80	1.07	13.73	6.60	0.16	1.89	5.04	3.40	1.64
CL06MI01	Olivine	CL15PS06	48.85	0.88	18.53	8.98	0.16	5.97	10.70	2.56	0.41
CL06MI02	Olivine	CL15PS06	51.14	1.01	18.83	9.14	0.15	4.63	10.23	3.21	0.53
CL06MI03	Olivine	CL15PS06	48.15	0.89	18.86	9.60	0.20	5.48	10.84	2.61	0.28
CV09EMI02	Olivine	CV15DJR09E	50.64	0.89	17.76	9.52	0.21	4.74	11.02	2.84	0.40
CV09EMI03	Olivine	CV15DJR09E	50.28	0.70	20.46	6.59	0.13	5.80	12.09	2.46	0.24
CV09EMI05	Olivine	CV15DJR09E	50.80	0.80	20.79	6.29	0.12	4.44	11.20	2.55	0.38

[a]H_2Ocalc is the corrected water contents based on SiO_2-H_2O trends (see Figure A2).[b]CO_2vbg is the CO_2 content of the melt inclusion corrected for vapor bubble growth using MIMiC (Rasmussen et al., in press). Melt inclusions with glass CO_2 contents below detection limits likely do not have significant amounts of CO_2 in their vapor bubbles. [cd]Tint and Ti are the intermediate and initial temperatures calculated using the olivine-melt thermometer of Putirka et al. (2007). The intermediate temperature is the temperature reflected by the measured melt inclusion composition. The initial temperature is the temperature reflected by the corrected composition of the melt inclusion (see Rasmussen et al., in press). [ef]Peq and Deq are the equilibrium pressure and depth (see text for details). [gh]Pi and Di are the initial (entrapment) pressure and depth (see text for details).

Geochemistry, Geophysics, Geosystems

10.1029/2019GC008882

Table 2
Continued

Sample	P_2O_5 (wt.%)	S (ppm)	Cl (ppm)	H_2O (wt.%)	H_2Ocalc (wt.%)[a]	CO_2 (ppm)	CO_2vbg (ppm)[b]	T_{int} (°C)[cd]	Ti (°C)[cd]	P_{eq} (MPa)[ef]	D_{eq} (km)[ef]	P_i (MPa)[gh]	D_i (km)[gh]
16IPE1BextMG01	0.21	56	595	0.06	2.5	0						54	2.3
16IPE1BextMG03	0.22	41	621	0.05	2.5	0						53	2.2
16IPE1BintPLAGMI01	0.28	120	664	1.96	2.8	b.d.				33	1.4		
16IPE1BextOLVMI04	0.12	697	698	1.04	3.4	0		956	1025	11	0.5	119	4.8
16IPE1BextOLVMI06	0.13	1533	530	2.41	3.7	0		987	1072	59	2.5	134	5.4
16IPE1BextPLAGMI02	0.12	123	916	1.82	2.1	0				29	1.3	40	1.7
16IPE1BextPLAGMI12	0.20	285	1095	2.01	2.7	0				34	1.5	61	2.5
16IPE1BextPLAGMI14	0.22	192	1137	1.13	2.5	0				12	0.6	52	2.2
16IPE1BextPLAGMI15B	0.21	215	1036	1.91	2.9	0				31	1.3	67	2.8
16IPE1BextPXMI07A	0.18	556	1008	3.07	3.1	0				72	3.0	74	3.1
16IPE1BextPXMI07B	0.20	b.d.	1145	N.D.	2.9	N.D.							
16IPE1BextPXMI07C	0.16	365	1006	N.D.	2.9	N.D.							
16IPE1BextPXMI07D	0.21	b.d.	823	N.D.	3.0	N.D.							
16IPE1BextPXMI08	0.16	146	889	2.54	2.3	0				52	2.2	47	2.0
16IPE1BextPXMI09	0.05	35	1515	2.52	2.2	0				51	2.1	43	1.8
16IPE1BextPXMI10	0.18	368	1009	1.70	2.8	0				25	1.1	65	2.7
16IPE1BextPXMI16A	0.19	190	1156	2.38	2.5	0				46	1.9	54	2.3
CL06MI01	0.13	2049	659	3.73	3.7	0		1024	1078	136	5.5	134	5.4
CL06MI02	0.17	1589	701	1.98	3.6	0		1012	1060	40	1.7	128	5.1
CL06MI03	0.13	2316	591	3.76	3.7	492	514	1080	1069	138	5.6	247	9.5
CV09EMI02	0.11	1106	692	N.D.	3.6	N.D.		1106	1096				
CV09EMI03	0.13	1319	547	2.82	3.6	361	430	1074	1071	80	3.3	223	8.7
CV09EMI05	0.13	1047	585	3.80	3.6	0		1016	1019	141	5.7	128	5.1

[a]H_2Ocalc is the corrected water contents based on SiO_2-H_2O trends (see Figure A2). [b]CO_2vbg is the CO_2 content of the melt inclusion corrected for vapor bubble growth using MIMiC (Rasmussen et al., in press). Melt inclusions with glass CO_2 contents below detection limits likely do not have significant amounts of CO_2 in their vapor bubbles. [cd]Tint and Ti are the intermediate and initial temperatures calculated using the olivine-melt thermometer of Putirka et al. (2007). The intermediate temperature is the temperature reflected by the measured melt inclusion composition. The initial temperature is the temperature reflected by the corrected composition of the melt inclusion (see Rasmussen et al., in press). [ef]Peq and Deq are the equilibrium pressure and depth (see text for details). [gh]Pi and Di are the initial (entrapment) pressure and depth (see text for details).

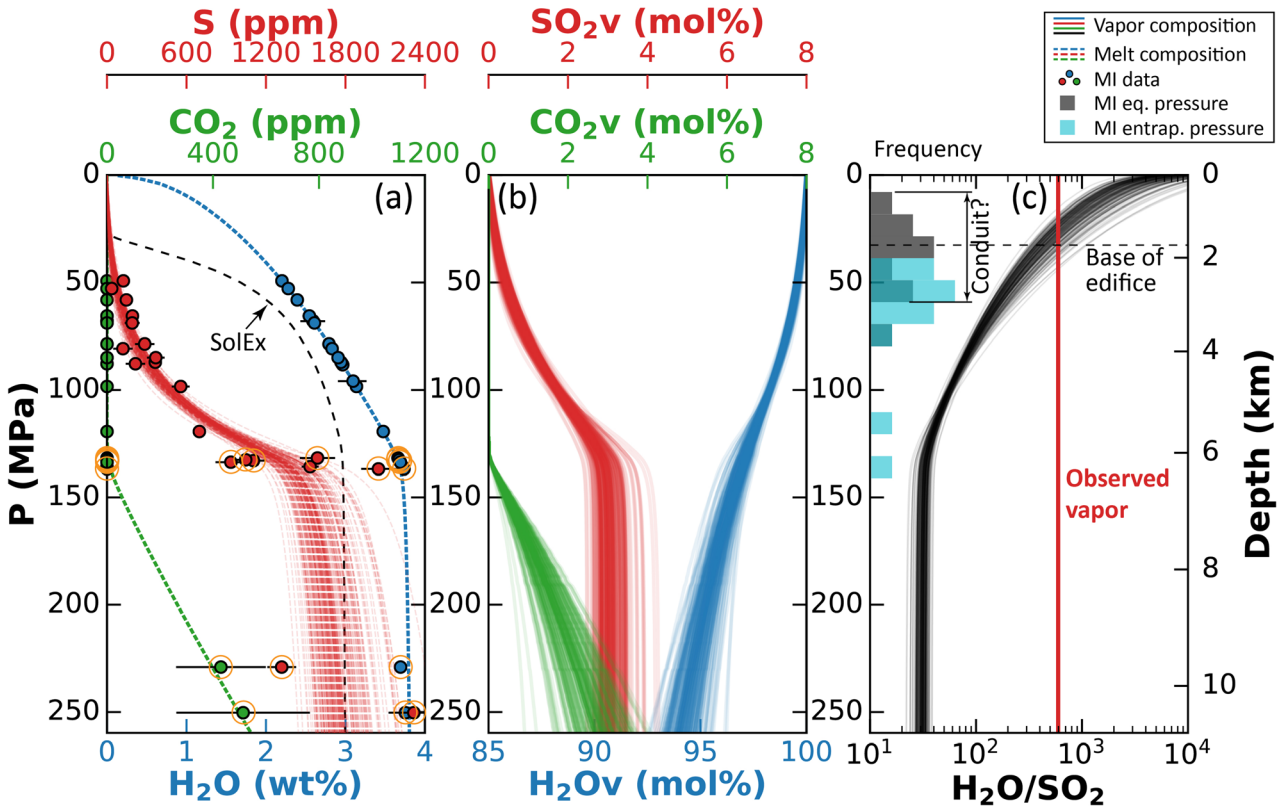

Figure 7. Degassing model showing results for 200 Monte Carlo simulations. (a) H_2O, CO_2, and S contents (by mass) of the modeled melt (dashed lines) and melt inclusions (scatter points). The circled melt inclusions are from the Holocene samples, and the remainder are from the 2016 sample. The H_2O and CO_2 contents of melt inclusions are corrected for diffusive loss of H^+ and vapor bubble growth, respectively. H_2O and CO_2 degassing are described by VolatileCalc (Newman & Lowenstern, 2002), and S degassing is described by our model. See text for details. Melt inclusions plot on dashed green and blue lines because their pressures were calculated based on their H_2O and CO_2 contents. Also shown is a degassing path for S calculated using SolEx (Witham et al., 2012), which is highly inconsistent with our melt inclusion data. (b) H_2O, CO_2, and SO_2 contents (molar) of the modeled vapor. (c) H_2O/SO_2 (molar) of the modeled (black lines) and measured (red line) vapor. (c, inset) Histogram of entrapment and equilibration pressures of melt inclusions erupted in 2016. A region of possible magma storage in a conduit is indicated. See text for details.

element compositions (e.g., Figure A2a and Table S4). Therefore, we suggest that the crystals are either coentrapped (e.g., large, opaque crystals, possibly magnetite), corrected for with PEC/PEM (e.g., small crystals in olivine-hosted melt inclusions in the 2016 sample), or minor in effect.

Major element contents of all melt inclusions occupy a wide compositional range, spanning from basaltic and basaltic andesitic compositions (48–56 wt.% SiO_2, Mg# 68–48) in olivine-hosted melt inclusions to andesitic and dacitic compositions (60–68 wt.% SiO_2, Mg# 49–32) in clinopyroxene- and plagioclase-hosted melt inclusions (Tables 2 and S4). Nearly the entirety of this compositional spectrum occurs in the 2016 sample. For all samples, melt inclusion compositional trajectories plot together and coincide with those of bulk rock samples (Figure A2a) but extend beyond bulk rock measurements to more silicic compositions. Compositional variation is well-described by MELTS models (Figure A2), indicating samples are consistent with origins along a single liquid line of descent. Volatile contents of melt inclusions are significantly variable (Figure 7). Olivine-hosted melt inclusions are typically more volatile-rich (700–2,320 ppm S; 3.4–3.7 wt.% corrected H_2O; ≤514 ppm corrected CO_2) than melt inclusions in other hosts (35–560 ppm S; 2.1–3.0 wt.% corrected H_2O; CO_2 below detection), and overall, S is anticorrelated with K_2O, providing evidence for degassing (S loss) during crystallization (K_2O increase), demonstrating that melt compositions shallower in the magmatic system are generally more evolved (i.e., higher K_2O concentrations; Figure A2c). S, H_2O, and CO_2 in all three samples form single trends consistent with degassing (Figure 7).

5. Discussion

5.1. The Relationship Between Gas Emissions and Volcanic Activity

Since 2011, Mount Cleveland has been in a state of nearly constant unrest. Activity has varied between periods of passive open-vent degassing and dome growth, interspersed with small explosive events and periods of quiescence (Werner et al., 2017). Since 2011, the cumulative radiative energy as measured by MODIS satellite has been observed to increase steadily each year with more radiance observed during periods of active dome growth (Figure A7, Werner et al., 2017). In contrast, there have been years with minimal to no SO_2 emission detected in OMI satellite measurements (Fioletov et al., 2016; Werner et al., 2017), demonstrating that the system is transient and that gas emissions change with time (Figure A7). The gas emission rates reported here (166–324 t/day) were made during a period of passive degassing during which the gas was observed to be streaming from an open vent that formed after May 2016, and the rates are within the range of those measured by OMI satellite for the period of 2005–2015 (annual averages were 0 to 456 t/day, with a decadal mean of 152 t/day SO_2) (Fioletov et al., 2016). SO_2 emissions in 2016 were lower than in 2015 (400–860 t/day SO_2), when measurements were made during, or up to 1 week after, a period of active dome growth (exact timing is unclear because no continuous measurements are available). Incandescence and high temperatures (650°C) measured by FLIR (Figure 4) were observed in the crater area in 2016 and suggested that magma was relatively close to the surface. Interestingly, in 2015 lower temperatures were measured in the summit area (450–600°C, Werner et al., 2017). This could be the combined result of ideal (clear, very windy) conditions in 2016 where the crater area was completely unobstructed by any gas in the crater, whereas in 2015 a significant amount of gas obstructed the view (see Werner et al., 2017). Alternatively, in 2015 a cooling carapace may have formed over the newly extruded dome, in contrast to 2016, when there was an open vent.

The composition of the gases suggests a relatively shallow magmatic source based on a high H_2O/SO_2 ratio, a low inferred CO_2/SO_2 ratio, and H_2S below the detection limits. Water vapor is very abundant in the atmosphere and its entrainment into volcanic plumes can complicate analysis of H_2O in MultiGAS measurements (Aiuppa et al., 2017), especially in dilute plumes measured using aircraft (Kelly et al., 2013). However, several lines of evidence indicate that entrainment of atmospheric water vapor did not affect the 2016 measurements. First, the agreement between two independent sensors measuring water vapor mixing ratios and RH was excellent (meaning the RH could be used to reproduce the water vapor mixing ratio), and the plume was noncondensing at the point of measurement. Second, the measurements indicate a volcanic H_2O source because the in-plume H_2O anomalies are spatially and temporally consistent with the SO_2 anomalies, and importantly, the in-plume H_2O anomalies at 1,650–1,800 m altitude are larger than background concentrations for air that could be reasonably entrained into the plume from any other elevation (Figures 3 and 4). Entrainment and transport of heterogeneous background air can lead to apparent in-plume anomalies for species that are abundant in the atmosphere, such as H_2O and CO_2 (Kelly et al., 2013). Yet in 2016 the vertical profiles demonstrate that the observed H_2O anomalies cannot be explained by entrainment of high-H_2O air from another altitude (i.e., ~1,350 m) because an associated consequence of such a process would be negative in-plume CO_2 anomalies on the order of 2–5 ppmv, which were not observed. Furthermore, the overall stability and stratification of the atmosphere observed during the airborne measurements indicates that vertical transport of ambient air parcels was limited.

Another possibility of obtaining elevated in-plume H_2O anomalies is from the evaporation of surficial or groundwater in the vent or surrounding area. While we acknowledge that this is indeed a likely process for explaining some of the water vapor flux, we do not find that this is a major contributor based on the following calculations. For instance, if we convert the range of water vapor flux based on the measured SO_2 flux and H_2O/SO_2 ratios (between 42,000 and 61,000 t/day, see below) into a volume, this results in ~4–6 $\times$ 10^4 m^3 of water vapor per day. If we then assume this water is sourced from the crater area (radius = 85 m, area of 2.27 $\times$ 10^4 m^2), because no water vapor anomalies were observed outside of this region, this then indicates that roughly 2–3 m of water would need to be remobilized each day. However, annual precipitation is only slightly over 1 m, which equates to daily rainfall of only 0.0027 m, making remobilization of shallow meteoric water from the vent region an unlikely explanation. To obtain a daily flux similar to what we observed would require all precipitation to infiltrate and be remobilized from a 15–22 km^2 region around the summit, which seems unlikely given the extent of this region. Furthermore,

the volcano lacks evidence of a significant groundwater system as no springs (hot or cold) have been observed on the island.

Without stable isotopic measurements of the fumarolic gas, it is impossible to estimate the amount of H_2O in the volcanic plume that originates from a deeper meteoric source (e.g., groundwater) or seawater that was incorporated into the volcanic gas stream at subvent depths. Infiltration of sea water to depths recorded by melt inclusions is unlikely because melt inclusions lack Cl enrichments that are expected if sea water assimilation occurred (Kent et al., 1999). However, this evidence does not preclude shallow seawater infiltration. Such water infiltration is a common feature in closed-vent volcanic environments where water is able to infiltrate the ground between the surface and the magmatic source, and the degree of primary water can be evaluated based on the isotopic signature of fumarolic samples (Giggenbach, 1992). For instance, at Augustine volcano in Alaska, USA, the isotopic signature of the gas suggested that the water vapor was a mix of magmatic water and seawater (Symonds et al., 1990). However, such observations are not ubiquitous. At White Island, New Zealand, a persistently degassing andesitic volcano in New Zealand, seawater was not an observed component in crater lake waters, fed by condensing fumarolic emissions in the main vent area. This is an important result considering there was evidence of seawater infiltration into the associated hydrothermal system neighboring the active vent (Christenson et al., 2017). Furthermore, recent modeling of Kilauea volcano has also highlighted the difficulty of meteoric waters infiltrating hot vents (Hsieh & Ingebritsen, 2019). Thus, the lack of ubiquitous water infiltration in the above examples, and more importantly our ability to replicate the measured H_2O/SO_2 ratio with a degassing-path derived from our melt inclusion data over a large range of pressures and depths (see below), lends confidence to the assertion of a dominant magmatic source for the measured H_2O. Nevertheless, we recognize that the measured bulk H_2O/SO_2 ratio is an upper limit for magmatic gas emitted from Mount Cleveland and that any contributions from meteoric sources would result in lower magmatic H_2O/SO_2 ratios.

While our measured bulk gas composition is more water-rich than in many high-temperature fumaroles that have been measured with Giggenbach bottles in arc settings (Fischer, 2008), the resulting H_2O/SO_2 is certainly not unprecedented. High-temperature fumarolic compositions for volcanoes across arcs worldwide have a median H_2O/S_2O ratio that clusters around 100, but some arcs, namely the Kuriles and the Cascades, have median H_2O/SO_2 ratios >250 (no high-temperature fumarolic analyses exist for the Aleutians) (Fischer, 2008). For instance, at Usu volcano, which lies at the junction between the NE Japan arc and the Kuril arc, H_2O/S_2O ratios up to 1,420 were measured in direct samples of 548–648°C fumaroles (Giggenbach & Matsuo, 1991). Furthermore, at Mount St. Helens, H_2O/S_2O ratios between 580 to 2,000 were measured by FTIR from the >600°C active vent in 2005 (Edmonds et al., 2008). Other examples include variable H_2O/SO_2 for a variety of volcanoes in a compilation of observations from Central America, where three have maximum H_2O/SO_2 values between 1,330 and 5,400. However, the conditions of each individual sample were not specified and the systems are quite different from Mount Cleveland (crater lakes, low temperature) (de Moor et al., 2017; de Moor et al., 2019). Another example of a specific volcano with no known hydrothermal degassing includes Bezymianny volcano (in Kamchatka), where an H_2O/SO_2 ratio of 580 was observed in fumarolic samples in 2007 (López et al., 2013). The high ratio here was attributed to shallow magma degassing. The same study reported a ratio of 26 in 2009, pointing to variability in the volcanic system, rather than external factors such as H_2O addition due to hydrothermal degassing or meteoric contributions. Finally, Kern et al. (2017) reported an H_2O/SO_2 ratio of 1,000 in the plume, and an emission rate of 250,000 t/day H_2O, from Sabancaya volcano just months prior to the 2016 eruption. At the time, the authors attributed the high value to evaporation of groundwater as it was heated by the rising magma column, but Moussallam et al. (2017) reported measurements of the gas composition from the previous year that showed a high-equilibrium temperature for the volcanic gas with no apparent contribution from a hydrothermal source.

We suggest that the overall high H_2O/SO_2 ratio from Cleveland is consistent with other volcanoes globally exhibiting open-system degassing of shallowly stored magmas. As shown below, our model predicts the more typical range of H_2O/SO_2 (e.g, ~100) at depths of 4 km, indicating that in the case of Cleveland in 2016, and Bezymianny in 2007, the source magmas were relatively shallow compared to most volcanic environments where direct gas samples have been obtained. Thus, existing fumarolic data may be biased toward systems with deeper magmas and water-rich compositions may become more common as the use of MultiGAS increases H_2O quantification from open-vent systems.

Finally, H_2O emission rates based on the measured H_2O/SO_2 ratio are between 42,000 and 61,000 t/day (Table 1). López et al. (2013) report a similar H_2O flux (45,000 t/day) for Bezymianny in 2007. CO_2 emission rates based on the measured SO_2 emission rates and a maximum CO_2/SO_2 ratio of 0.7 would have had to be on the order of 130–190 t/day at the time of sampling to be detected. The CO_2/SO_2 ratio here is calculated from maximum CO_2 that would have resulted in no CO_2 above the detection limit of the instrument, given the measured SO_2 content of the plume. The CO_2 emission rate could of course be lower than this estimate (see below). Similarly, the maximum H_2S emission based on the H_2S/SO_2 detection limit (0.048) would have been ~8 t/day. The low CO_2 emission and the low C/S ratio reported here suggests the vapor originated from magma that had previously degassed CO_2, which is consistent with shallow magma depths and the low CO_2 concentrations in the 2016 melt inclusions.

5.2. Magma Storage Depths

Although gas compositions suggest a shallow source for magmatic degassing, further constraints on the magmatic plumbing system come from melt inclusions. H_2O and CO_2 contents in melt inclusions can be related to depth by modeling vapor saturation pressures and applying a crustal density model (Figure A3). This assumes the magma is under lithostatic (i.e., pressure of overlying rock), not magmastatic (i.e., pressure of overlying magma), pressure, but this assumption makes little difference. At shallow depths, where a conduit might exist and an argument for magmastatic pressure can be made, the densities in our velocity model are low (<2,200 kg/m^3 at <5-km depth) and similar to densities of intermediate-evolved (Lesher & Spera, 2015) magmas unless a substantial vapor phase is present. Thus, at shallow depths, magmastatic and lithostatic models yield similar results. Saturation pressure is predominantly a function of melt H_2O and CO_2 contents (Moore, 2008), which is why melt inclusions plot directly on H_2O and CO_2 curves in Figure 7a. As discussed in section 3, melt inclusions studied here have experienced postentrapment processes that modified H_2O and CO_2 contents. Using the approach of Rasmussen et al. (2018), such postentrapment modifications can be leveraged to derive two depths from melt inclusions: entrapment depth and equilibration depth. Entrapment depth indicates the depth of melt inclusion formation. This is calculated using inferred values for the originally entrapped H_2O and CO_2 contents, obtained by correcting melt inclusions for diffusive loss of water and vapor bubble growth. Entrapment depths can reflect either regions of magma storage (e.g., Colman et al., 2015) or simply where degassing-induced crystallization occurred upon ascent (e.g., Lloyd et al., 2013). The second is equilibration depth, which describes the last depth of storage prior to eruption. This depth is derived from the measured H_2O contents of a melt inclusion, determined by finding the pressure at which those H_2O contents fall on a modeled degassing path. This is typically the H_2O saturation pressure for open systems because in this degassing scenario CO_2 completely degasses before significant degassing of H_2O occurs (Newman & Lowenstern, 2002). Diffusive water loss is assumed to have occurred mostly during shallow storage, instead of during magma ascent or posteruptive cooling. Here, the basis for this assumption is the shallow entrapment depths of the melt inclusions (Figure 7), which suggest the maximum path length for ascent is short and thus ascent times are minimal. Additionally, the dacitic host has a cool magmatic temperature, implying slow diffusion of H^+ (Ferriss et al., 2018), and we find no relationship between melt inclusion diameter and water content, which is expected for melt inclusions that lose water diffusively upon ascent (Rasmussen et al., 2017). Furthermore, some of the hosts are plagioclase feldspar, which equilibrate H^+ over timescales of days or more (Johnson & Rossman, 2013). Therefore, we suggest the equilibration depths reflect the region where melt inclusions were stored for at least days to weeks prior to eruption. We note that our use of the term "storage" does not necessarily imply that melt inclusions stagnated at a single depth for the timescale of equilibration. Rather, melt inclusions existed in a shallow part of the system where diffusive water loss occurred, and the depth of this region is approximated by the equilibration depth. We assign a 20% uncertainty to pressure and depth estimates from melt inclusions, which was determined by calculating the relative standard deviation of saturation pressures calculated for a magma with 2.5 wt.% H_2O (~3 km depth) using various volatile solubility models (Figure A5).

Both entrapment and equilibration depths of melt inclusions from the 2016 bomb point to a shallow depth of magma residence, whereas melt inclusions from our more mafic (and older) samples record somewhat greater depths for entrapment. Most of the 2016 melt inclusions were entrapped at <4 ± 0.8 km depth (below the summit), except for the two olivine-hosted melt inclusions entrapped at ~6 ± 1.2 km depth. Olivine-hosted melt inclusions from the Holocene samples have entrapment depths between 6 ± 1.2 and

11 ± 2.2 km. For both the 2016 and Holocene samples, more mafic melt inclusions have greater entrapment depths. The 2016 melt inclusions have equilibration depths that range between 0.5 ± 0.1 and 3.0 ± 0.6 km, consistent with the existence of a shallow magmatic system over this depth range. We focus our attention on the equilibration depths of just the 2016 melt inclusions because they are the most reflective of the modern plumbing system. The large range of equilibration depths implies a vertically extensive plumbing system, which is consistent with a conduit-like geometry. The melt inclusions from the more mafic Holocene samples have variable equilibration depths mostly between 2 ± 0.4 and 6 ± 1.2 km. The greater equilibration depths relative to 2016 melt inclusions indicate that preeruptive magma storage was different.

The depths of magmatic processes can also be inferred from geophysical data. Seismicity at Cleveland has been measured by two seismic stations (CLES and CLCO) maintained by the Alaska Volcano Observatory since 2014, and by a year-long campaign deployment of 6–12 broadband seismometers from summer 2015 to summer 2016 (Janiszewski et al., 2020; Power et al., 2017). Cleveland's seismic activity from 2015–2016 is generally characterized by relatively low rates of midcrustal (~2–8 km BSL, or 3.7–9.7 below the summit) high-frequency (HF) or volcano-tectonic (VT) earthquakes related to brittle failure of rocks, and by moderate rates of shallow, low-frequency (LF) or long-period (LP) seismicity during background periods (Power et al., 2017). The LP events cannot be located due to their indistinct body phase arrivals but are thought to be located at shallow depths (within the edifice) because they record most strongly on stations near the summit and decrease in amplitude with distance. The observation of LP seismicity at shallow depths below Mount Cleveland is thought to be the result of movement of fluids, either magma or gas, in this region (Chouet & Matoza, 2013), and thus is consistent with the concept of a fluid-filled conduit inferred from melt inclusions. Also important to note is that analysis of the source processes driving the occasional small Vulcanian explosions observed at Mount Cleveland shows that they are related to long-period expansion and contraction of the conduit at a depth range of 1.4 to 1.7 km below the summit (Haney et al., 2019), which is close to the location where the predicted vapor composition (from melt inclusions) matches that of the measured H_2O/SO_2 (~1.4 km; Figure 6c).

A notable exception to the measured background seismic activity is a swarm of earthquakes that was recorded in late-August/September 2015, which were located directly beneath Cleveland's summit at depths of approximately 4–8 km BSL, or 5.7–9.7 below the summit (Power et al., 2017). This cluster of VT seismicity may reflect a transfer of magma and/or fluids from the midcrust into the shallow system based on the increased occurrence of a LP seismic swarm that followed shortly after the VT swarm events (Power et al., 2017). At even greater depth, *S* wave velocity anomalies resolved from teleseismic receiver functions indicate a low velocity zone, interpreted to be a vertically-elongated region of magma storage, exists below the region of VT seismicity. The depth of this anomaly ranges from 10–20 km BSL, or minimally 11.7 km below the summit (Janiszewski et al., 2020). The approximate radius of this storage region is 2.5 km and the low velocities observed suggest a long-lived stable system as opposed to recently injected dikes that have yet to thermally equilibrate. Thus, geophysical data point to active magmatic processes at multiple levels beneath the edifice and to regions where magma is transported through the entire crust.

In summary, equilibration depths of 2016 melt inclusions provide evidence for a shallow storage system between 0.5 ± 0.1 to 3.0 ± 0.6 km, largely within the volcanic edifice, which fed the 2016 summit eruption. Observations of LP seismic events shallow in the system are consistent with the movement of magma or gas in this region, and Vulcanian explosion source depths of 1.4–1.7 km are located within this same zone. Deeper magmatic processes cause sporadic VT events between 3.7 to nearly 10 km below the summit, which is the region where many melt inclusions were first entrapped. A swarm of earthquakes, thought to be a magmatic recharge event, was observed in the deepest part of this zone (5.7 to ~10 km) in 2015. At ~12 km depth, teleseismic data show a vertically elongated and long-lived region of magma (or mush) storage, but the melt inclusions studied did not sample magmas from this region.

5.3. A Degassing Model for Mount Cleveland

Open-vent volcanoes like Mount Cleveland, where the magmatic system is connected to the atmosphere through an open vent, are generally characterized by persistent gas and thermal emissions, elevated

background seismicity rates, and frequent mild eruptive activity (Rose et al., 2013). Many of the world's most active volcanoes have an open vent and produce strong, nearly continuous, but variable gas emissions that have been measured using MultiGAS and remote techniques (Aiuppa et al., 2009). Open-vent volcanoes often support an open-system, where gas is allowed to separate from magmas, leading to periods of passive degassing between eruptive periods, termed excess degassing (Shinohara, 2008). Excess degassing of SO_2 is a prominent characteristic of Mount Cleveland based on the observations of persistent degassing and low volumes of eruptive products for nearly all recent eruptions (Werner et al., 2017). While persistent, degassing is variable. On an annual basis SO_2 emissions vary dramatically and are not always correlated to heat flux (Figure A7). Interannual variability in degassing, only qualitatively assessed since the deployment of a web camera in 2014, also exists. As documented in the 2014–2016 annual reports published by the Alaska Volcano Observatory (Cameron et al., 2017; Dixon et al., 2017), "robust" or "vigorous" steam plumes have typically following episodes of regional seismicity, tremor, or dome growth. In between these episodes the degassing is described as "minor steam plumes" at a frequency of ~1–10 times per month. These observations are consistent with the comparison of the 2015 SO_2 emissions with the present study, where more SO_2 was observed to be emitting during a period of higher volcanic activity in 2015. It is important to note that volcanic CO_2 was not detected in either campaign suggesting that the volcanic system was not open to great depths where a CO_2-charged magma might be located.

Additional evidence for open-system processes comes from petrologic data. The analyzed sample erupted in 2016 likely originated from a system that was open with respect to crystals, vapor, and melt. In the single volcanic bomb examined, crystal compositions vary significantly and include olivine (Fo72–81), clinopyroxene (Mg#73–78), and plagioclase (An63–82). Crystals have morphological (e.g., dissolution) and chemical (e.g., concentration gradients) signs of disequilibrium, indicating not all crystals formed in their host melt. Melt inclusions within those crystals span basaltic to dacitic melt compositions. Melt inclusions have high water contents and low values of CO_2, implying that the system is open with respect to volatiles (i.e., open-system degassing path; Figure A6; Newman & Lowenstern, 2002). This chemical trend is the opposite of what is expected for CO_2-fluxing (e.g., Rasmussen et al., 2017), indicating this process is not important at Cleveland. Additionally, the high observed ratio of H_2O/SO_2 in volcanic gases could not be achieved by modeling a closed system.

We modeled the degassing path of Cleveland magmas from the surface (with the summit at 1,730 m being the baseline elevation) to 12-km depth based on open-system dynamics (Figure 7, Table S6). Modeled melt volatile contents were determined by performing regressions on melt inclusion data from all samples, resulting in a close fit between predicted and measured values (Figure 7a). Other models (e.g., SolEx, also open-system, Witham et al., 2012) were not able to reproduce the S degassing path of melt inclusions. The H_2O-CO_2-pressure relationships in SolEx are equivalent to those in our model (calculated using VolatileCalc) because both models are based on solubility relationships described by Dixon (1997). Therefore, we think the discrepancy is due to the predicted behavior of S. The offset is likely a consequence of SolEx employing vapor-melt partitioning relationships for S that are calibrated with a small number of experimental data for a limited range of melt composition, temperature, pressure, and fO_2. The accompanying vapor (Figure 7b) at ~12-km depth is predicted to have ~95 mol% H_2O and roughly equal amounts of CO_2 and S. Owing to its low solubility, CO_2 becomes completely degassed in the melt at roughly the same depth as the onset of significant S and H_2O degassing (~6 km). The H_2O/SO_2 modeled for the system reaches ~100 at a depth of ~4 km (Figure 7c). At shallower depths, degassing increases the H_2O/SO_2 ratio of the vapor exponentially.

We present two end-member scenarios that could produce the measured H_2O/SO_2 of ~600 in 2016 (Figure 8). In Scenario 1, we consider the possibility that a magma body lies within the edifice of Mount Cleveland at a fixed depth of ~1.4 ± 0.3 km below the summit (or at 20–40 MPa). This magma body could produce gas at the required ratio, but could it sustain the SO_2 flux? Werner et al. (2017) suggested at least half of the overall magma budget over the 5-year period of that study (i.e., 2.4–7.3 Mm^3) likely intruded to a shallow depth beneath the edifice, but did not erupt, based on the long-term heat budget. This magma, when constrained by the measured S contents in this study, would degas in a matter of days assuming an average emission rate of 324 t/day SO_2. Thus, a much larger volume of magma would

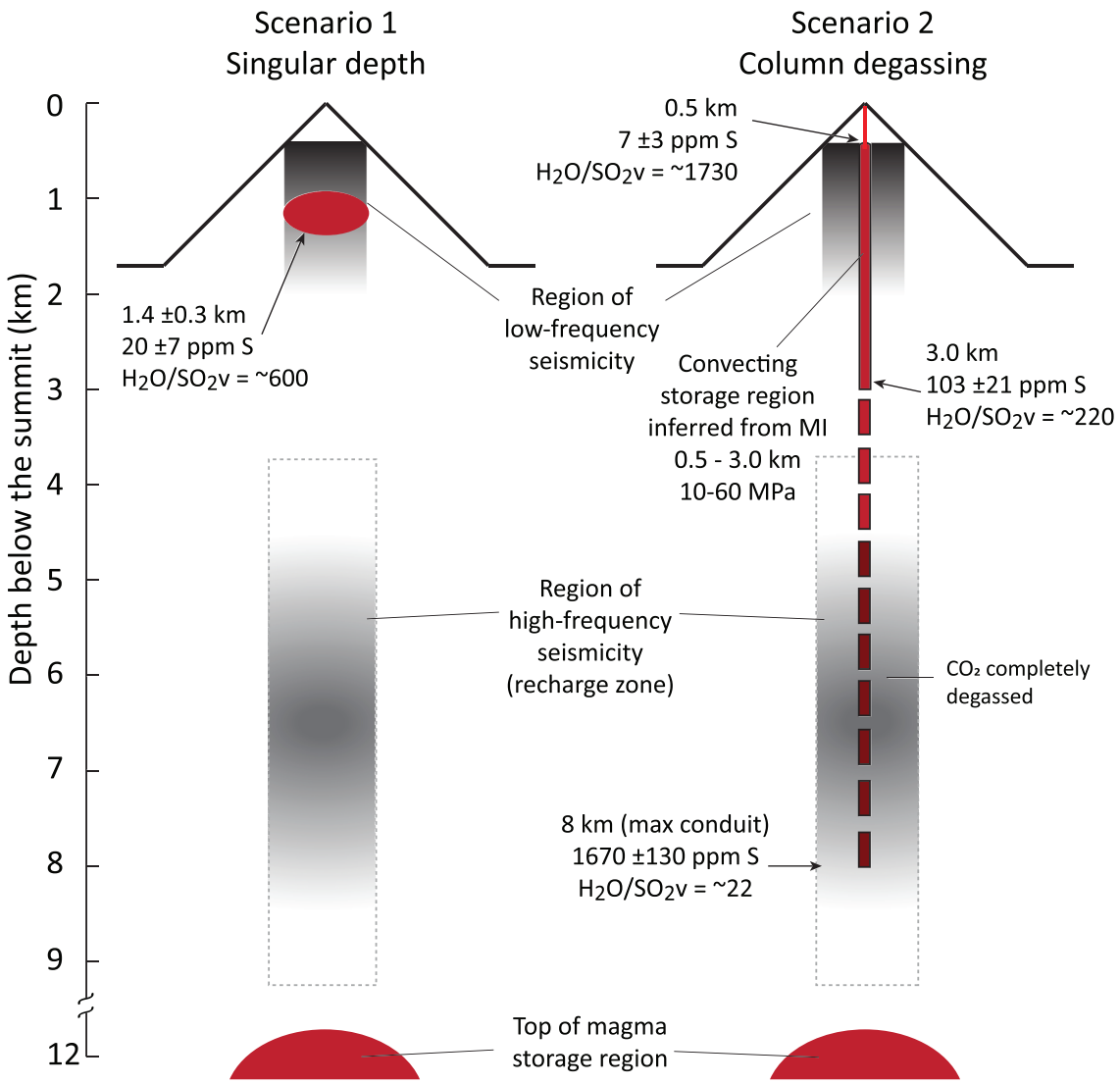

Figure 8. End-member scenarios of the magmatic plumbing system at Cleveland volcano. In these schematics, bright red indicates where magma is present. The thin line near the summit in Scenario 2 represents a path for volcanic gases to escape the magma body starting at 0.5 km depth prior to the 2016 eruption (minimal thermal anomalies detected in the months prior to these explosions, Figure A7). The magma storage region at ~12 km depth is proposed by Janiszewski et al. (2020) based on teleseismic imaging of the middle-to-lower crust. In Scenario 1, degassing occurs at a discrete depth. In Scenario 2, degassing occurs over a range of depths, and the observed vapor is a mixture of vapor degassed throughout the column. Our data supports scenario 2. See text for details.

be required to produce this level of emission over the long-term, as OMI measurements suggest. In the event of appreciable shallow magma storage, one might expect measurable deformation of the edifice or more laterally extensive seismicity. Neither are observed at Cleveland. In the periods that have been observed by satellite (2004–2009, Lu & Dzurisin, 2014, and 2011–2012, Wang et al., 2015), there has been a lack of measurable deformation in InSAR data at Mount Cleveland, including periods prior to volcanic eruptions. The lack of measurable deformation led Lu and Dzurisin (2014) to infer that no appreciable shallow magma storage exists at Mount Cleveland, and for Wang et al. (2015) to assert that, in the lead up to the 2011 eruption, the ascending magma passed through a preexisting conduit system. Thus, we reject the possibility that large volumes of magma are being stored at shallow levels within the edifice (i.e., in the upper 1.7 km).

A different scenario, but similar to Scenario 1, is that the bulk gas is produced through the mixing of a partially degassed silicic magma located in the upper middle crust with a volatile rich mafic magma that

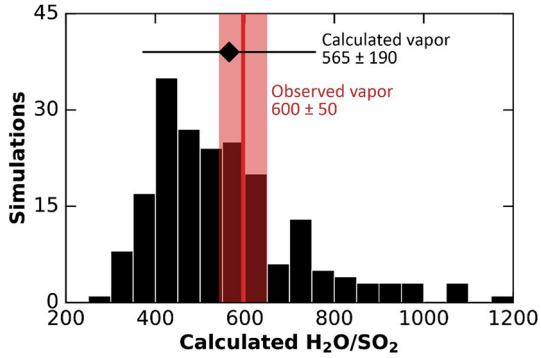

Figure 9. Modeled H_2O/SO_2 composition of a mixed vapor degassed over the melt inclusion equilibration pressure range (10–60 MPa) (0.5 to 3.0 km depth) for 200 Monte Carlo simulations. The red line and shaded area are the average and standard deviation of the measured H_2O/SO_2 ratio. The black diamond indicates the average modeled H_2O/SO_2, and the uncertainty is the 1σ standard deviation.

periodically injects from deeper in the system. It is commonly suggested that arc andesites, like the 2016 bulk eruptive product of Cleveland, form in this way (Reubi & Blundy, 2009). In this scenario, the observed bulk H_2O/SO_2 could be produced by release of H_2O from a shallow, S- and C-poor evolved magma, and the majority of the S degasses from the mafic magma upon interaction of the two magmas. However, we find such a model unlikely for our period of observation for several reasons. First, the observed 2016 melt compositions, represented by melt inclusions and matrix glasses erupted in 2016, do not form a linear array expected of mixing (Figure A8). Rather, they form a kinked trend that lies off the mixing line, and we interpret this to be the product of crystallization. Second, deeply sourced magma would supply CO_2 in addition to S, and the lack of measurable CO_2 during the 2015 and 2016 field campaigns indicates that we did not detect degassing of deeper magmas. Additionally, other observations at Mount Cleveland such as the lack of observed deformation over any studied time period related to eruptive activity (Lu & Dzurisin, 2014; Wang et al., 2015), persistent thermal anomalies, and small lava dome formation and drain back (Werner et al., 2017) are not typical of volcanoes with closed crustal reservoirs that experience mafic injections. For instance, Redoubt Volcano, Augustine Volcano, and Mount St. Helens are volcanoes having large, viscous lava-dome eruptions, measurable deformation, and minimal thermal anomalies and degassing between eruptions. This discussion is not to suggest that recharge to or through the midcrust does not happen and that no magma residence could occur in this region, but rather that there is simply minimal evidence of this occurring during 2016 (Figure 7). As previously noted, seismic data indicate that recharge of a shallow system (0.5–3 km depth) by magmas originating in the middle to lower-crust occurs episodically, and they are required to explain the long-term SO_2 flux with our preferred model, as is discussed below. However, we have no measurements to support the existence of such a shallow midcrustal reservoir being the source of the eruptive products or gas in 2016.

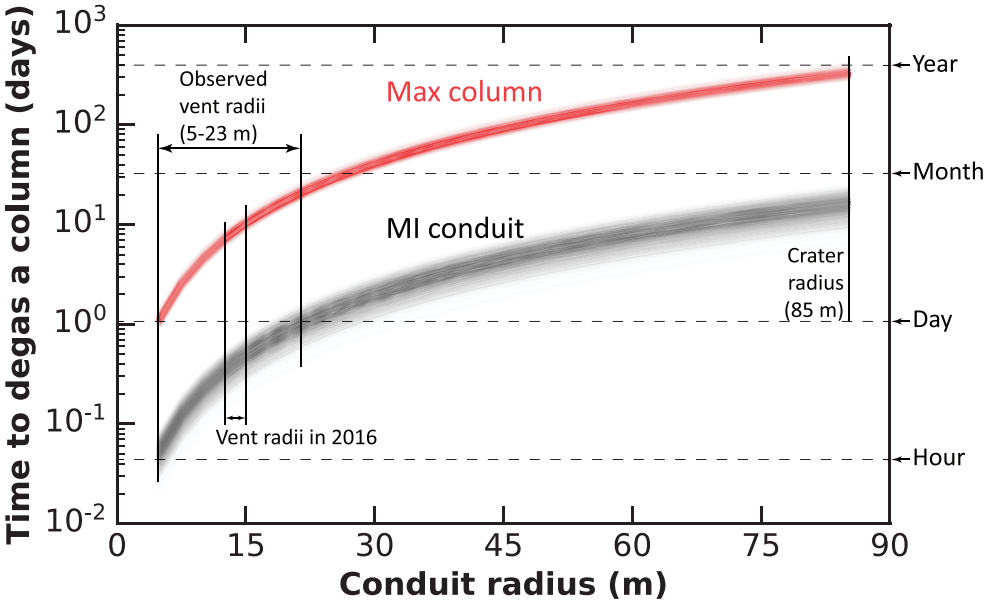

Figure 10. Modeled degassing rates, for magma columns of different heights and diameters, required to explain the observed SO_2 flux (324 t/day). The degassing rate is the number of times per day an entire column of magma must be degassed. Plotted are results from 200 Monte Carlo simulations for two different pressure ranges (i.e., column heights), the shading demonstrates the multiple solutions. MI conduit is for a pressure range of 10–60 MPa (i.e., 0.5–3.0 km depth), which is defined by 2016 melt inclusion equilibration pressures. Max column is for a pressure range of 1–200 MPa (i.e., 0–8 km depth), which is the maximum pressure range that produces the measured H_2O/SO_2 of the vapor in some Monte Carlo results (see Figure A4). See the text for an explanation of the model.

In scenario 2, our preferred model, gas emissions are produced by magmas ascending, degassing, and crystallizing at a range of depths in a vertically extensive system, perhaps a conduit (Figure 8). The gases measured at the surface are a mixture of those released across the entire depth range. In the previous section, we outlined evidence for a vertical column based on the eruptive products and seismic observations (Janiszewski et al., 2020; Power et al., 2017). We constrain the possible dimensions of the vertical system using the equilibration depths of melt inclusions erupted in 2016, which is representative of the last depth of storage for the melt inclusions prior to eruption. Most equilibration pressures are 10 ± 2 to 60 ± 12 MPa, which equates to ~0.5 ± 0.1 to 3.0 ± 0.6 km depth beneath the summit. The average modeled H_2O/SO_2 composition of a mixed vapor degassed over this pressure range for 200 Monte Carlo simulations is 565 ± 190 (Figure 9). This overlaps remarkably well with the measured range of 600 ± 50 in the measured gases, but the mode of solutions is shifted to slightly lower values (~500) of H_2O/SO_2 (Figure 9). Lower magmatic H_2O/SO_2 would be expected if meteoric sources were influencing the measured gas ratio, thus this effect would strengthen the correlation. We note that a continuum of column dimensions can produce a vapor with an H_2O/SO_2 of 600 in our model (Figure A9). The maximum column height that can reproduce an H_2O/SO_2 of 600 extends from 0 to 8 km depth (Figure A9), which we later use as a column height endmember when considering S flux (i.e., "Max column" in Figure 10 is 0–8 km and is compared to the "melt inclusion (MI) conduit," which extends from 0.5 to 3.0 km). We favor the 0.5–3.0 km column model because it is consistent with melt inclusion equilibration pressures and the source depths of the Vulcanian explosions (Haney et al., 2019). We note that a simplification in our model for this scenario is that magma exists in a continuous, vertical cylinder. The basis for this assumption is that a cylindrical conduit can explain the mechanics of dome-forming eruptions (Melnik et al., 2005), and this model works well to explain summit observations. The assumption may be appropriate for short columns at shallow depths (i.e., "MI conduit"). However, for longer columns, reaching more significant depths (i.e., "Max column"), this assumption should be viewed as a simplification in order to approximate a system that might not be continuous or have a simple geometry. This assumption affects calculations of gas composition and flux, which are influenced by shape and continuity of the storage region.

5.4. Total Magma Supply and Evidence for Convection

We recognize that the measurements here represent a snapshot in time, but the SO_2 emission rates measured in 2016 are in fact representative of the long-term rates (Fioletov et al., 2016). Thus, we can pair the measured emission rates with initial magmatic volatile contents from our most primitive samples to calculate a maximum total magma supply needed to produce the measured SO_2 fluxes over the long term, and compare that estimate with estimates derived from the heat flux in previous studies (Werner et al., 2017). The initial S content of the magma is based on the maximum observed S content of the Holocene melt inclusions (2,320 ppm), which was trapped at ~10-km depth. If all of this S is eventually released from this magma (assuming a basalt with a density estimated at 2,600 kg/m^3) upon ascent, and if the emission rates we measured (166–324 t/day SO_2) are representative of the long-term average as noted above, this implies degassing of between 5 and 9.8 Mm^3 of magma each year. As expected, this value is significantly higher than the estimate of magma reaching the shallow subsurface derived from the heat output of the volcano, which was between 0.88 to 2.6 Mm^3 per year between 2011 and 2015 (Werner et al., 2017). Furthermore, the magma supply rate calculated from the sulfur budget (0.2–0.3 m^3/s) is much higher than the average proposed magma supply rate based on the heat budget (0.055 m^3/s, Werner et al., 2017). The reason the heat-based magma volumes and supply rates are much lower than the S-based estimates is because the thermal signature only represents magma that is very close to, or has erupted onto, the surface, whereas the S-based budget considers the entire, degassing column which may extend to considerable depth. The long-term heat output measured at the volcano has stayed relatively stable over the entire period from 2011–2018, thus temporal variability does not affect the estimates (Figure A7). Werner et al. (2017) calculated that between 1.9 to 5.8 Mm^3 of magma extruded as lava domes between 2011 and 2015, which equates to 0.38 to 1.16 Mm^3 per year. These calculations indicate that only up to ~8% of the total magma supply erupts on average, with 92% of the magma remaining at depth, resulting in an intrusive-to-extrusive ratio of ~13:1. This is typical for subduction-related magmatism as estimated by Crisp (1984).

In assessing the thermal budget of Mount Cleveland, Werner et al. (2017) proposed conduit convection to a shallow level as the process that could sustain the persistent thermal activity observed at Mount Cleveland since 2011. Over the five-year period of observation, pervasive thermal anomalies were observed in MODIS satellite data that, when compared to degassing and thermal output from other volcanoes worldwide, implied a persistent presence of a near-surface magma in the conduit at Mount Cleveland. This near-surface magma degases, and the thermal anomalies observed (in satellite, or FLIR images) must be due to either the gas itself, lava at the surface, or hot rock in the shallow conduit visible in the open vent. Our melt inclusion data indicate that crystalizing magma is located at depths as shallow as 500 m, based on equilibration depths of 2016 samples, but evidence for magma crystallization at shallower depths has not been documented thus far (note also that few thermal anomalies were observed in the months prior to the 2016 explosions, Figure A7). Observations of dome morphology and frequent draining of magma from the vent in the central crater both suggest that a low-viscosity magma exists at Mount Cleveland (Fink & Griffiths, 1998), despite the dacitic melt composition reported here. For these reasons, magma convection in the conduit to the near surface was deemed a plausible mechanism to maintain the continual thermal output without lava extrusion between periods of dome growth.

We can use our degassing model paired with the Scenario 2 geometric end-member (magma residing in a column/conduit) over a range of physical constraints such as the magma column heights and diameters to constrain the rate of convection (Figure 10). This requires the assumption that the entire column of magma convects in a single cell, which is a simplification, but it provides a first-order constraint on the process. We first constrain the modeled column height based on the melt inclusion equilibration depth range ("MI Conduit"; Figure 10), that is, from 0.5 to 3.0 km depth below the summit. Column radii were allowed to vary within a range based on visual observation of vent radii (5–23 m), but as a maximum, we modeled scenarios with radii of up to 85 m, which is equivalent to the crater radius of Mount Cleveland (Figure 10). This exercise shows that if the column has a radius of the largest observed vent radius (23 m), that the volume of the magma column existing over the range of the melt inclusion equilibration depths would degas at least once a day (Figure 10), resulting in an inferred minimum ascent rate of 5.8 cm/s assuming a complete (e.g., two lengths of conduit) overturn. This is over 5 times the ascent rate inferred for Popocatepetl volcano in Mexico (Witter et al., 2005), a rate which is unrealistic. If, however, the conduit is larger (up to 85 m), then the column would degas over ~2–10 days, resulting in lower, and perhaps more reasonable, ascent rates (0.6 to 2.9 cm/s) (Figure 10). Although magma convection in narrow conduits is proposed at basaltic volcanoes worldwide, such as Villarica where a 5-m diameter conduit was proposed over an arbitrary 1-km length (Witter et al., 2005), there are fewer examples for more silicic systems. As discussed by Kazahaya et al. (1994), larger conduit radii predicted for more silicic systems can easily compensate for the higher viscosities observed in more silicic magmas. At Sakurajima, an andesitic volcano, convection was physically plausible with conduit radii of 20–50 m where viscosity was estimated at $10^{3.4}$ Pa·s at 1000°C (Kazahaya et al., 1994). At Cleveland, we predict viscosities would likely be 10^{4-5} Pa·s (crystal free) assuming 900°C and using an evolved melt inclusion composition and the model of Giordano et al. (2008). The viscosity would perhaps be 10–100 times greater if a crystal fraction of 50% is assumed, using equation 5.9 of Lesher and Spera (2015) and assuming values of 3 for chlorine and 0.64 for the maximum packing fraction. Similarly, at Satsuma-Iwojima, a rhyolitic volcano (10^6 Pa·s at 1000°C for the degassed magma), a radius of 25 m was required to degas the 600 t/day observed (Shinohara, 2008). Although our predicted radii are consistent with the more silicic volcanoes mentioned, the period over which the column degasses is short (weeks at most), requiring either a larger dimension of the plumbing system at depth, or an additional source of deeper magma to sustain the SO_2 flux over timescales greater than weeks. We speculate that even though the range of observed vent dimensions is reasonable for convection to occur in light of other studies, they are not necessarily a reliable measure of the conduit dimensions with increasing depth, which is unconstrained. Data from the 2015–2016 seismic deployment show that VT seismicity clusters in a ~500-m-wide radius at ~6-km depth and extends out to 2.5-km radius at greater depth (Janiszewski et al., 2020), indicating the possibility of a widening plumbing system. These data were also used to derive a velocity model in the upper conduit at Mount Cleveland, which was seismically slow compared to other volcanoes in the Aleutians (e.g., Seguam). Slow velocities could be caused by substantial quantities of partial melt at depth, which may be more than can be contained in a relatively narrow

conduit. Alternatively, slow velocities could be due to other factors such as unconsolidated volcanic deposits, or an abundance of fractures in the edifice.

The time to degas a convecting magmatic volume (Figure 10) becomes more reasonable if it is connected to or resupplied from a larger magmatic body at depth. Our results suggest the maximum column height that can produce a vapor with a bulk H_2O/SO_2 that matches our measured ratios is 8 km ("Max column"; Figure 10), which covers nearly the entire depth over which seismicity was observed during detailed seismic monitoring in 2015–2016 (Power et al., 2017). In this case, the time to degas the magma within the conduit increases from days to a year. Although maintaining convection over a relatively narrow conduit over a great depth is likely unrealistic, this exercise shows that sustaining persistent degassing (visual plumes) and thermal anomalies observed over multiple years at Mount Cleveland requires recharge by deeply derived, gas-rich magma, and during such periods one would expect lower H_2O/SO_2 and measurable CO_2 emissions. It is important to note that the gas signature measured in this study reflects a shallow process (0.5–3 km depth) at an isolated point in time, whereas a longer-term time series of gas composition and flux would shed light on the deeper processes of recharge. An isolated recharge event has been hypothesized for the midcrustal seismic swarm in August–September 2015 (Power et al., 2017), which followed initial fieldwork (Werner et al., 2017). The lack of measurable CO_2 during the 2015 and 2016 field campaigns indicates that we did not detect degassing of deeper magmas. To date, the measurements represent magma where CO_2 has previously been degassed and is evidenced from both the degassing measurements and melt inclusion data.

We use our degassing model to calculate a representative CO_2 flux for the period of measurement. At pressures less than 140 MPa (~6-km depth), CO_2 is nearly completely degassed in the melt and does not contributed significantly to the gas composition, such that any CO_2 in a deeply derived gas is diluted when mixing with more shallow gases that are dominated by H_2O and SO_2. Thus, in the case of "MI Conduit" (0.5–3 km), CO_2 is completely degassed from magmas at these depths (Figure 7), and no CO_2 emission is expected. However, if we consider the "Max column" case (0–8 km), our model suggests a maximum emission rate of 50 t/day CO_2. This estimate is lower than, and thus consistent with, the upper limit of 130–190 t/day suggested above based on the instrument detection limits. For this hypothetical 8-km column, the model predicts a C/S ratio on the order of 0.2. The low CO_2 emissions and C/S ratio are consistent with behavior observed at other open-system volcanoes where deeply derived gas escapes from magma deep within the subsurface. Evidence for excursions to higher C/S in the hours to months prior to increased volcanic activity has been documented at multiple systems worldwide such as Villarica, Etna, Stromboli, and Turrialba volcanoes (Aiuppa et al., 2007; Aiuppa et al., 2009; Aiuppa et al., 2017; de Moor et al., 2016; Werner et al., 2019, and references therein). This type of behavior illustrates that CO_2 release at these volcanoes is pulsatory and related to fresh magma recharge at significant depth. An obvious limitation of our work at Mount Cleveland is that only two short-duration (~1 hr) measurements were made at the volcano, roughly 1 year apart. Analysis of a longer record of gas composition and emissions at Mount Cleveland would result in a significantly more robust model of the system.

6. Conclusions

We combined volcanic gas emission rates and compositions with melt inclusion data to develop a simple empirical degassing model for H_2O-CO_2-S based on mass balance for the magmatic system at Mount Cleveland volcano in Alaska. Average measured emissions of SO_2 were between 166 and 324 t/day using SO_2 camera and airborne techniques on 24 and 25 July 2016, respectively, and they are similar to the long-term average measured in OMI satellite data. Average H_2O emission rates based on a (maximum) H_2O/SO_2 ratio of ~600 $\pm$ 53 measured using airborne techniques were between 42,000 and 61,000 t/day, respectively. The H_2O/SO_2 ratio is consistent with a shallow magmatic source and also with high-temperature fumarolic compositions from a number of volcanoes globally, but it is expected to vary in time. Melt inclusion volatile contents from the 2016 sample show direct evidence of magmas residing between 0.5 $\pm$ 0.1 and 3.0 $\pm$ 0.6 km depth below the summit, which is consistent with the depth of explosion sources derived from geophysical studies. The deepest 2016 melt inclusions were sourced from 6 km below the summit, which is consistent with a zone of volcano-tectonic seismicity where a recharge event was inferred to have occurred in July–August 2015. Degassing over a 0.5–3.0 km depth range (below the

summit), based on melt inclusion equilibration depths, can produce a gas with the observed H_2O/SO_2, perhaps indicating that a conduit system exists over this depth range. Initial estimates of time to degas a magma column from 0.5 to 3.0 km depth based on measured emission rates is rapid (~1 day) if the conduit radius is constrained by vent dimensions This unrealistic degassing rate indicates that a larger conduit radius or frequent recharge from a deeper magma source is required to sustain the long-term SO_2 emission. Ultimately, the specific geometry of the conduit and/or magma reservoirs at depth remain unconstrained, but the degassing budget and the most primitive melt inclusions suggest that on average between 5 and 9.8 Mm^3, a year is required to degas to sustain the long-term SO_2 flux. This estimate is higher than a magma budget previously derived from heat flux data, and together the data indicate an intrusive-to-extrusive ratio of ~13:1 (or 8% of the magma erupts). Volcanic CO_2 was below detection limits of the MultiGAS instrumentation, but modeling of CO_2 degassing indicates a maximum emission rate of 50 t/day and a C/S molar ratio of 0.2, assuming a maximum 8 km depth, which is the maximum column length that can produce a vapor with the measured H_2O/SO_2 ratio. The SO_2 emission, heat flux, and melt inclusion data together support a model where magma convected in a column that extends from near the surface to at least 3 km depth prior to the 2016 eruption. However, replenishment of this column by a deeper, less degassed, magma likely residing below 8 km, is required to sustain heat and SO_2 fluxes over months-to-years timescales.

Appendix A.

The following figures (Figures A1–A9) provide additional support for the data and modeling presented here.

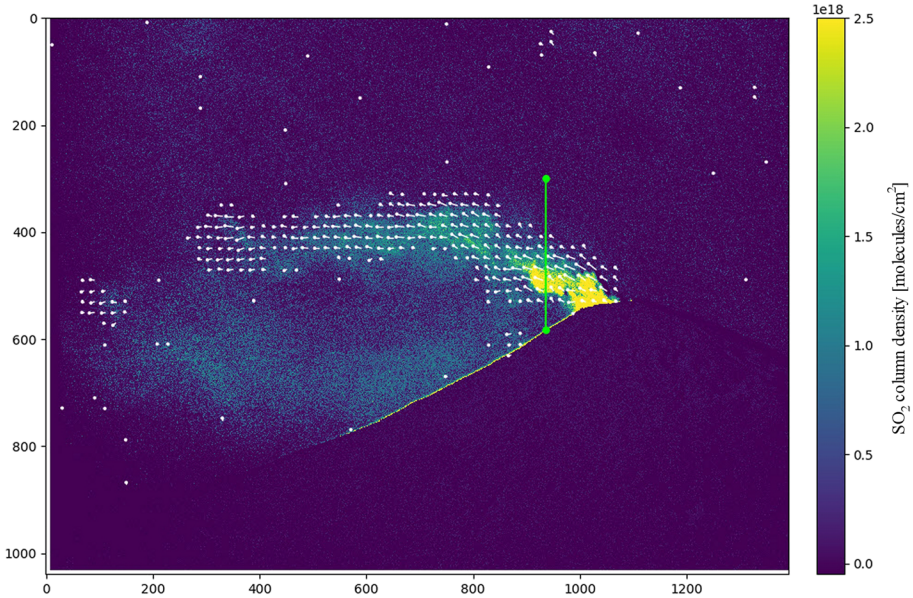

Figure A1. SO_2 camera image showing the configuration used for measurement. The vertical line indicates where the SO_2 emission rate was calculated.

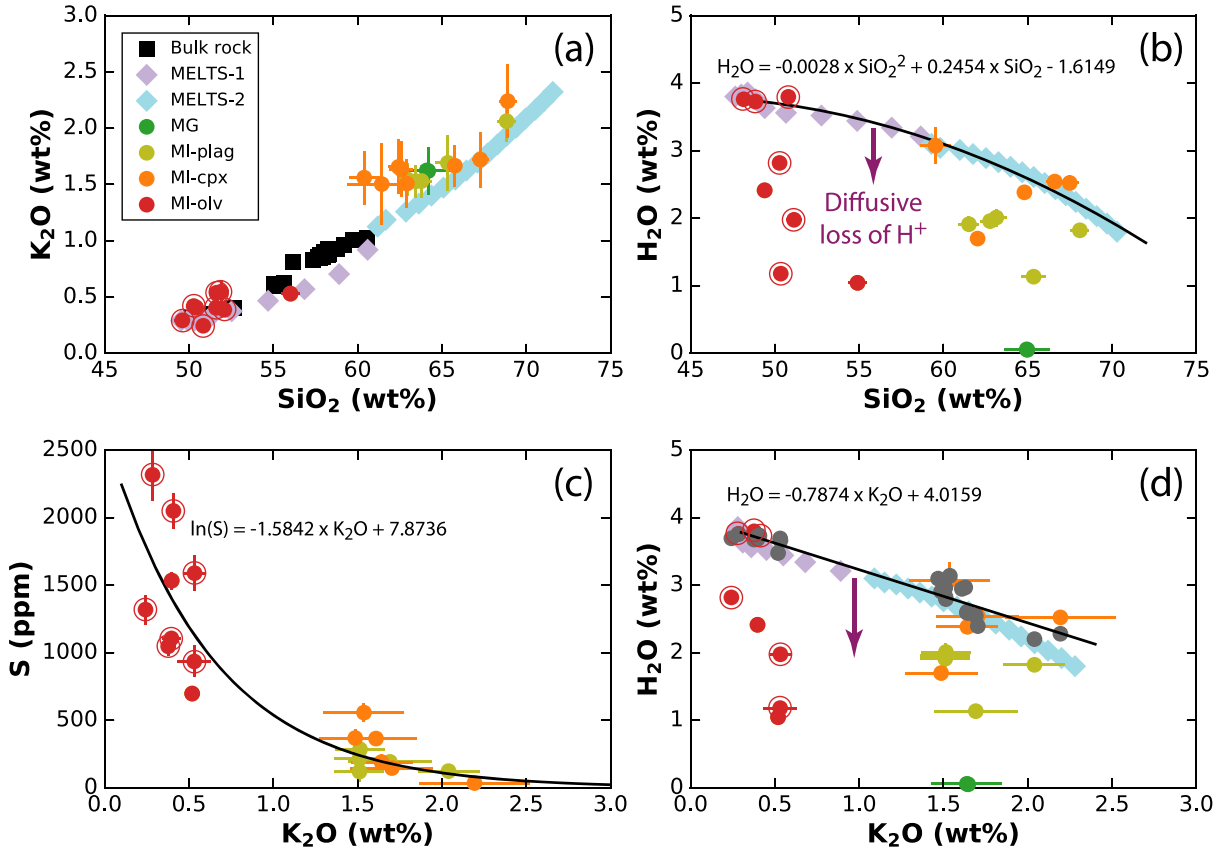

Figure A2. Major element and volatile compositions of melt inclusions. Melt inclusions from the Holocene samples are circled, and those from the 2016 sample are not circled. (a) Major element plot showing consistent liquid lines of descent in melt inclusions, matrix glasses, bulk rocks, and MELTS models. MELTS-1 is modeled with a cooling rate of 8 bar/°C. MELTS-2 is modeled using 6 bar/°C. (b) H_2O and SiO_2 contents of melt inclusions, matrix glasses, and MELTS models. A regression of the MELTS model results is shown, which was used to calculate the initial (entrapped) H_2O contents of melt inclusions. The lack of correlation between H_2O and SiO_2 contents of melt inclusions is clear evidence for diffusive loss of H^+ (purple arrow), but a few melt inclusions follow the expected trend for ascent, degassing, and crystallization. (c) S and K_2O contents of melt inclusions with a log-linear regression. (d) H_2O and K_2O contents of melt inclusions, matrix glasses, and MELTS models. Melt inclusions corrected for diffusive loss of H_+ using the equation in Figure A2c are shown in gray. A linear regression of the corrected melt inclusion data is shown.

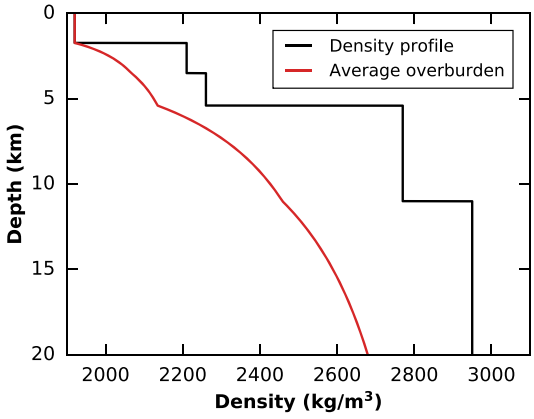

Figure A3. Density versus depth calculated for Mount Cleveland. A one-dimensional velocity model used for earthquake location at Cleveland was obtained by inverting 119 well-picked hypocenters using VELEST (Kissling et al., 1994) and trial and error runs of the earthquake location program hypocenter (Lienert & Havskov, 1995) were used to minimize the RMS error of *P* and *S* wave arrivals (Power et al., 2017). This density model was derived from the one-dimensional seismic velocity using the relationships established between seismic velocity and density by Barton (1986).

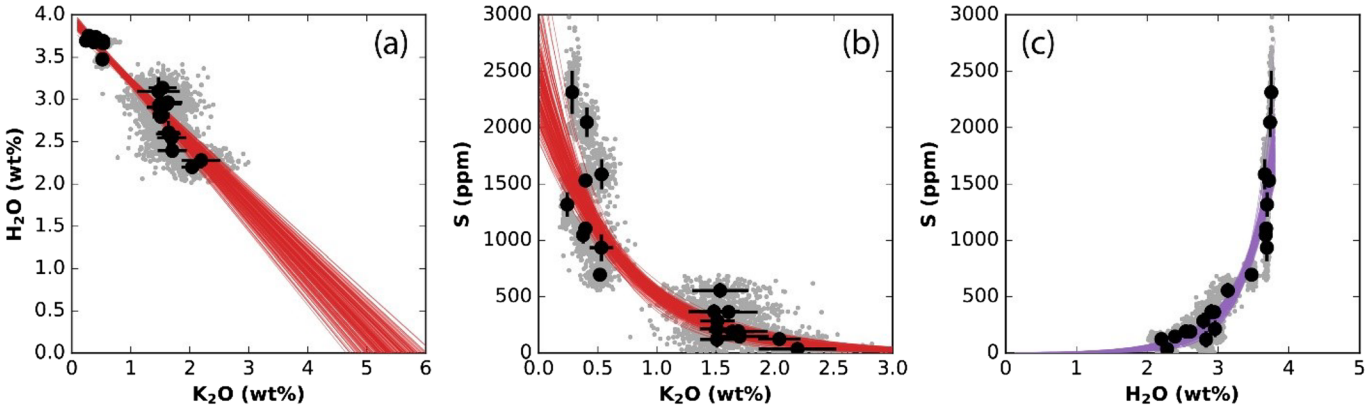

Figure A4. Degassing model results for 200 Monte Carlo simulations. Input melt inclusion data (black circles) and resampled melt inclusion data (gray circles) are shown. Red lines in (a) and (b) are regressions of the resampled melt inclusion data for each of the 200 Monte Carlo simulations. Violet lines in (c) are the results of the degassing model.

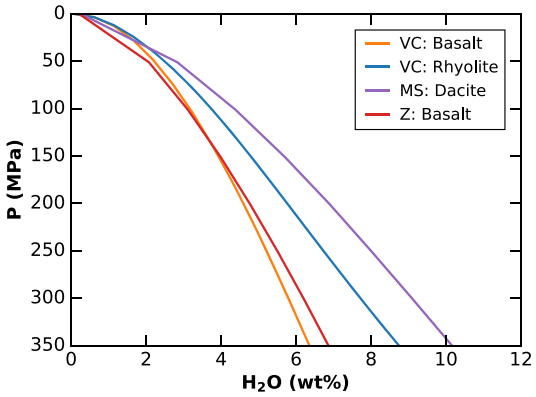

Figure A5. Water solubility calculated for basalt-rhyolite melt compositions using several different solubility models: VC (Newman & Lowenstern, 2002), MS (Ghiorso & Gualda, 2015), and Z (Zhang et al., 2007). Melt compositions used in modeling are from the MELTS modeling results.

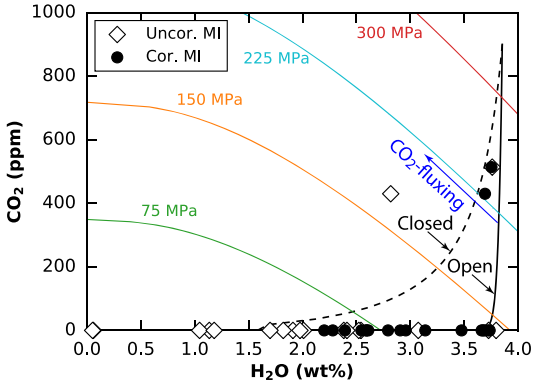

Figure A6. H_2O and CO_2 contents of measured ("Uncor.") and H_2O-loss-corrected (Cor.) melt inclusions (MI). See text for information on H_2O-loss correction. The solid and dashed black lines are modeled open system and closed system, respectively, degassing paths, calculated using VolatileCalc (Newman & Lowenstern, 2002). Both assume a temperature of 1,100°C and melt composition of 49 wt.% SiO_2. The closed-system path was calculated to start with 1 wt.% of exsolved fluid. The starting CO_2 content (900 ppm) was selected arbitrarily because the initial CO_2 contents of the magmas are unknown. The path of isobaric CO_2-fluxing is shown (e.g., Rasmussen et al., 2017).

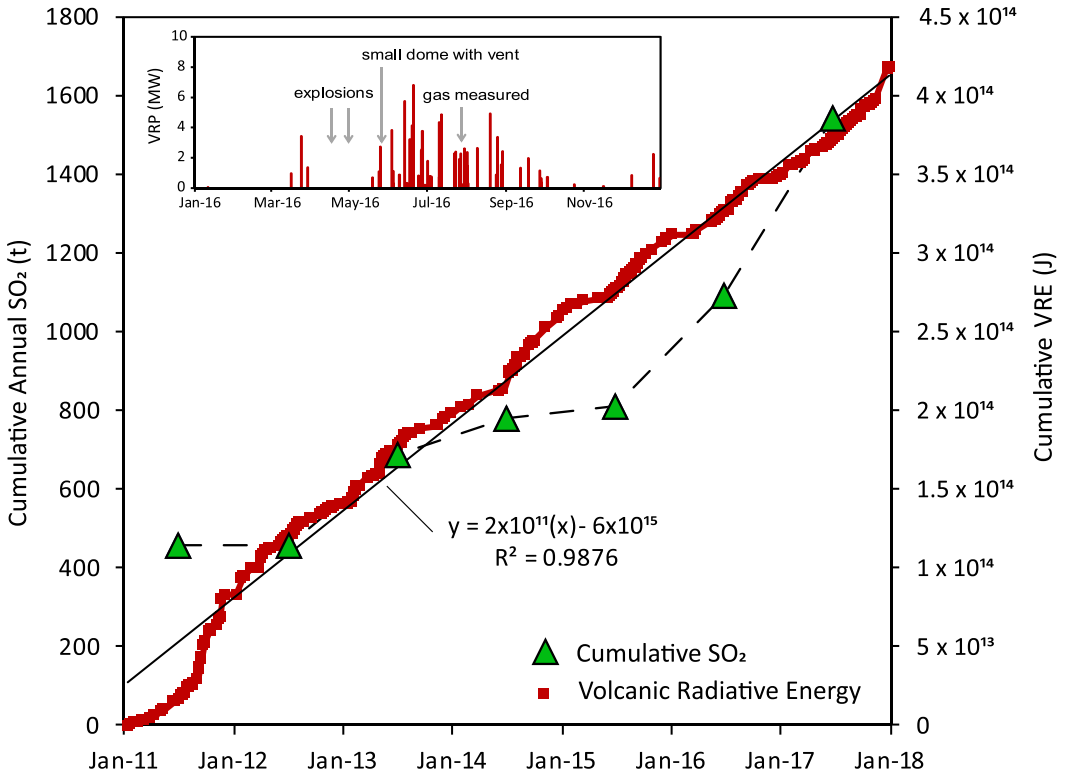

Figure A7. Cumulative volcanic radiative energy (VRE, in joules) measured by MIROVA (MODIS satellite) and annual SO_2 emissions measured by OMI satellite over the period of 2011 to 2018 (in t). The annual heat flux shows a relatively steady increase over the period of measurement, whereas SO_2 emissions vary year to year. The inset shows the thermal output for 2016, which is typical of many years (Werner et al., 2017), but shows that few thermal anomalies were observed in the months prior to the 2016 explosion. Volcanic radiative energy data provided by Diego Coppola (Università degli Studi di Torino, Italy), and OMI data provided by Simon Carn (Michigan Tech University, USA) for 2016–2017, and Fioletov et al. (2016) for 2011–2015.

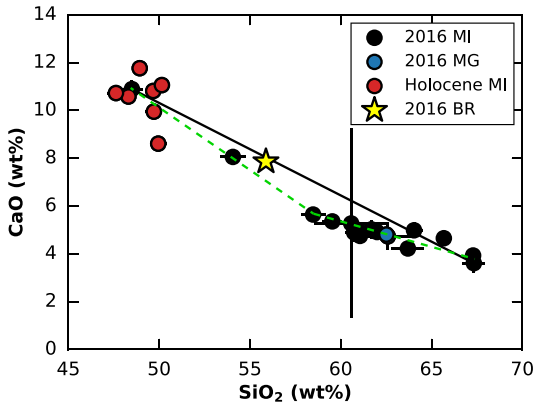

Figure A8. SiO_2 and CaO contents of the 2016 and Holocene melt inclusions (MI) and the 2016 bulk rock (BR) and matrix glasses (MG). The water content for all compositions is calculated using the H_2O-K_2O relationship in Figure A2, and all compositions have been normalized to 100%. Glass compositions (i.e., MG and MI) represent melt compositions. The black, solid line shows mixing between the most evolved and most primitive 2016 melt compositions. It is notable that the 2016 melt compositions do not fall on this trend, which would be expected if magma mixing created the observed melt compositions. Instead, melt compositions follow a kinked path (approximated by dashed green line) that we interpret to be the result of crystallization. The bulk composition of the 2016 sample plots near the solid, black mixing trend, and also near an observed melt composition. The bulk sample contains crystals with textural and chemical signs of disequilibrium, indicating that addition (or perhaps removal) of crystals may have influenced the observed bulk composition.

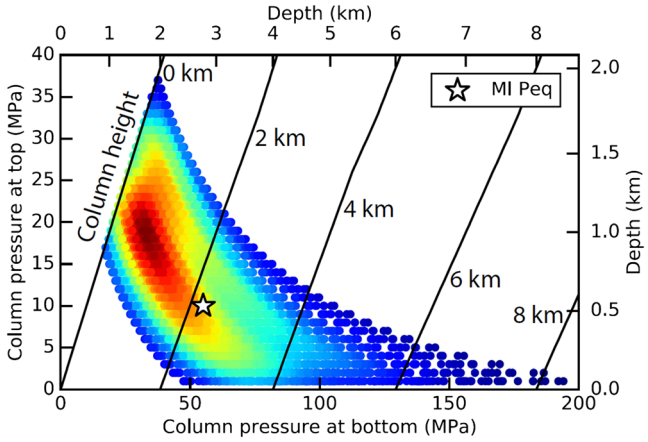

Figure A9. Scatter density plot of magma column locations that produce a vapor with an H_2O/SO_2 equivalent to that of the observed vapor. Plotted are the column configurations for each of the 200 Monte Carlo simulations that produce a vapor with an H_2O/SO_2 of 596. Warmer colors indicate column configurations with a greater number of solutions. Column height is shown with black lines. The range of equilibration pressures (Peq) of melt inclusions erupted in 2016 is represented by a star.

Acknowledgments

The authors would like to thank Maarten de Moor, Brendan McCormick Kilbride, Jake Lowenstern, and one anonymous reviewer for their thoughtful comments that improved this manuscript, and to the National Science Foundation (EAR-1456939 to D. C. R. and EAR-1456814 to T. P.) and the Alaska Volcano Observatory for funding this work. The authors would like to thank the crew of the Maritime Make and Dan Leary for piloting the Bell 407 helicopter. Data Availability Statement All DOAS and MultiGAS data presented and interpreted in this study are available at the USGS ScienceBase (https://doi.org/10.5066/P9DRMV0U). Petrologic samples collected for this study are registered with SESAR (https://www.geosamples.org/). Geochemical data related to these samples can be found in the EarthChem (https://www.earthchem.org/) database and have the following titles and urls: (1) Melt inclusion data for Cleveland volcano (https://doi.org/10.26022/IEDA/111539), (2) Matrix glass data for Cleveland volcano (https://doi.org/10.26022/IEDA/111540), and (3) Bulk rock data for Cleveland volcano (https://doi.org/10.26022/IEDA/111541).

References

Aiuppa, A., Bertagnini, A., Metrich, N., Moretti, R., Di Muro, A., Liuzzo, M., & Tamburello, G. (2010). A model of degassing for Stromboli volcano. *Earth and Planetary Science Letters*, *295*(1-2), 195–204. https://doi.org/10.1016/j.epsl.2010.03.040

Aiuppa, A., Bitetto, M., Francofonte, V., Velasquez, G., Parra Claudia, B., Giudice, G., et al. (2017). A CO_2-gas precursor to the March 2015 Villarrica volcano eruption. *Geochemistry, Geophysics, Geosystems*, *18*, 2120–2132. https://doi.org/10.1002/2017GC006892

Aiuppa, A., Burton, M., Caltabiano, T., Giudice, G., Guerrieri, S., Liuzzo, M., et al. (2010). Unusually large magmatic CO_2 gas emissions prior to a basaltic paroxysm. *Geophysical Research Letters*, *37*, L17303. https://doi.org/10.1029/2010GL043837

Aiuppa, A., Federico, C., Giudice, G., Giuffrida, G., Guida, R., Gurrieri, S., et al. (2009). The 2007 eruption of Stromboli volcano: Insights from real-time measurement of the volcanic gas plume CO_2/SO_2 ratio. *Journal of Volcanology and Geothermal Research*, *182*(3–4), 221–230. https://doi.org/10.1016/j.jvolgeores.2008.09.013

Aiuppa, A., Federico, C., Giudice, G., & Gurrieri, S. (2005). Chemical mapping of a fumarolic field: La Fossa crater, Vulcano Island (Aeolian Islands, Italy). *Geophysical Research Letters*, *32*, L13309. https://doi.org/10.1029/2005GL023207

Aiuppa, A., Moretti, R., Federico, C., Giudice, G., Gurrieri, S., Liuzzo, M., et al. (2007). Forecasting Etna eruptions by real-time observation of volcanic gas composition. *Geology*, *35*(12), 1115–1118. https://doi.org/10.1130/G24149A.1

Allard, P., Aiuppa, A., Bani, P., Métrich, N., Bertagnini, A., Gauthier, P. J., et al. (2016). Prodigious emission rates and magma degassing budget of major, trace and radioactive volatile species from Ambrym basaltic volcano, Vanuatu island arc. *Journal of Volcanology and Geothermal Research*, *322*, 119–143. https://doi.org/10.1016/j.jvolgeores.2015.10.004

Allard, P., Burton, M., Sawyer, G., & Bani, P. (2016). Degassing dynamics of basaltic lava lake at a top-ranking volatile emitter: Ambrym volcano, Vanuatu arc. *Earth and Planetary Science Letters*, *448*, 69–80. https://doi.org/10.1016/j.epsl.2016.05.014

Barton, P. J. (1986). The relationship between seismic velocity and density in the continental crust—A useful constraint? *Geophysical Journal International*, *87*(1), 195–208. https://doi.org/10.1111/j.1365-246X.1986.tb04553.x

Beirle, S., Sihler, H., & Wagner, T. (2013). Linearisation of the effects of spectral shift and stretch in DOAS analysis. *Atmospheric Measurement Techniques*, *6*(3), 661–675. https://doi.org/10.5194/amt-6-661-2013

Bluth, G. J. S., Shannon, J. M., Watson, I. M., Prata, A. J., & Realmuto, V. J. (2007). Development of an ultra-violet digital camera for volcanic SO_2 imaging. *Journal of Volcanology and Geothermal Research*, *161*(1-2), 47–56. https://doi.org/10.1016/j.jvolgeores.2006.11.004

Bogumil, K., Orphal, J., Homann, T., Voigt, S., Spietz, P., Fleischmann, O., et al. (2003). Measurements of molecular absorption spectra with the SCIAMACHY pre-flight model: Instrument characterization and reference data for atmospheric remote-sensing in the 230–2380 nm region. *Journal of Photochemistry and Photobiology A: Chemistry*, *157*(2–3), 167–184. https://doi.org/10.1016/S1010-6030(03)00062-5

Bull, K. F., & Buurman, H. (2013). An overview of the 2009 eruption of Redoubt volcano, Alaska. *Journal of Volcanology and Geothermal Research*, *259*, 2–15. https://doi.org/10.1016/j.jvolgeores.2012.06.024

Burgisser, A., Alletti, M., & Scaillet, B. (2015). Simulating the behavior of volatiles belonging to the C-O-H-S system in silicate melts under magmatic conditions with the software D-compress. *Computers & Geosciences*, *79*, 1–14. https://doi.org/10.1016/j.cageo.2015.03.002

Burton, M., Allard, P., Muré, F., & La Spina, A. (2007). Magmatic gas composition reveals the source depth of slug-driven Strombolian explosive activity. *Science*, *317*(5835), 227–230. https://doi.org/10.1126/science.1141900

Cameron, C. E., Dixon, J. P., Neal, C. A., Waythomas, C. F., Schaefer, J. R., & McGimsey, R. G. (2017). *2014 volcanic activity in Alaska—Summary of events and response of the Alaska Volcano observatory*, U.S. Geological Survey.

Campion, R., Delgado-Granados, H., & Mori, T. (2015). Image-based correction of the light dilution effect for SO_2 camera measurements. *Journal of Volcanology and Geothermal Research*, *300*, 48–57. https://doi.org/10.1016/j.jvolgeores.2015.01.004

Carn, S., Fioletov, V., McLinden, C., Li, C., & Krotkov, N. (2017). A decade of global volcanic SO_2 emissions measured from space. *Scientific Reports*, *7*(1), 44,095. https://doi.org/10.1038/srep44095

Cashman, K. V. (2004). Volatile controls on magma ascent and eruption. *Washington DC American Geophysical Union Geophysical Monograph Series*, *150*, 109–124.

Chouet, B. A., & Matoza, R. S. (2013). A multi-decadal view of seismic methods for detecting precursors of magma movement and eruption. *Journal of Volcanology and Geothermal Research*, *252*, 108–175. https://doi.org/10.1016/j.jvolgeores.2012.11.013

Christenson, B. W., White, S., Britten, K., & Scott, B. J. (2017). Hydrological evolution and chemical structure of a hyper-acidic spring-lake system on Whakaari/White Island, NZ. *Journal of Volcanology and Geothermal Research*, *346*, 180–211. https://doi.org/10.1016/j.jvolgeores.2017.06.017

Colman, A., Sinton, J. M., & Wanless, V. D. (2015). Constraints from melt inclusions on depths of magma residence at intermediate magma supply along the Galápagos Spreading Center. *Earth and Planetary Science Letters*, *412*, 122–131. https://doi.org/10.1016/j.epsl.2014.12.007

Danyushevsky, L., & Plechov, P. (2011). Petrolog3: Integrated software for modeling crystallization processes. *Geochemistry Geophysics Geosystems*, *12*, Q07021. https://doi.org/10.1029/2011GC003516

Danyushevsky, L. V., McNeill, A. W., & Sobolev, A. V. (2002). Experimental and petrological studies of melt inclusions in phenocrysts from mantle-derived magmas: An overview of techniques, advantages and complications. *Chemical Geology*, *183*(1-4), 5–24. https://doi.org/10.1016/S0009-2541(01)00369-2

De Angelis, S., Fee, D., Haney, M., & Schneider, D. (2012). Detecting hidden volcanic explosions from Mt. Cleveland Volcano, Alaska with infrasound and ground-coupled airwaves. *Geophysical Research Letters*, *39*, L21312. https://doi.org/10.1029/2012GL053635

de Moor, J. M., Aiuppa, A., Avard, G., Wehrmann, H., Dunbar, N., Muller, C., et al. (2016). Turmoil at Turrialba volcano (Costa Rica): Degassing and eruptive processes inferred from high-frequency gas monitoring. *Journal of Geophysical Research: Solid Earth*, *121*(8), 5761–5775. https://doi.org/10.1002/2016JB013150

de Moor, J. M., Kern, C., Avard, G., Muller, C., Aiuppa, A., Saballos, A., et al. (2017). A new sulfur and carbon degassing inventory for the southern central American volcanic arc: The importance of accurate time-series datasets and possible tectonic processes responsible for temporal variations in arc-scale volatile emissions. *Geochemistry, Geophysics, Geosystems*, *18*, 4437–4468. https://doi.org/10.1002/2017GC007141

de Moor, J. M., Stix, J., Avard, G., Muller, C., Corrales, E., Diaz, J. A., et al. (2019). Insights on hydrothermal-magmatic interactions and eruptive processes at Poás volcano (Costa Rica) from high-frequency gas monitoring and drone measurements. *Geophysical Research Letters*, *46*, 1293–1302. https://doi.org/10.1029/2018GL080301

Dean, K. G., Dehn, J., Papp, K. R., Smith, S., Izbekov, P., Peterson, R., et al. (2004). Integrated satellite observations of the 2001 eruption of Mt. Cleveland, Alaska. *Journal of Volcanology and Geothermal Research*, *135*(1–2), 51–73. https://doi.org/10.1016/j.jvolgeores.2003.12.013

Dixon, J. E. (1997). Degassing of alkalic basalts. *American Mineralogist*, *82*(3–4), 368–378. https://doi.org/10.2138/am-1997-3-415

Dixon, J. P., Cameron, C., McGimsey, R. G., Neal, C. A., & Waythomas, C. (2015). *2013 volcanic activity in Alaska—Summary of events and response of the Alaska Volcano Observatory*. U.S. Geological Survey Scientific Investigations Report 2015–5110.

Dixon, J. P., Cameron, C. E., Iezzi, A. M., & Wallace, K. (2017). *2015 volcanic activity in Alaska—Summary of events and response of the Alaska volcano observatory*. 2017–5104, Reston, VA.

Doukas, M. P. (2002). *A new method for GPS-based wind speed determinations during airborne volcanic plume measurements* (Open-file report 02-395), U.S. Geological Survey, David A. Johnston Cascades Volcano Observatory.

Edmonds, M., McGee, K. A., & Doukas, M. P. (2008). *Chlorine degassing during the lava dome-building eruption of Mount St. Helens*, 2004-2005, 1750–27. Reston, VA.

Ferriss, E., Plank, T., Newcombe, M., Walker, D., & Hauri, E. (2018). Rates of dehydration of olivines from San Carlos and Kilauea Iki. *Geochimica et Cosmochimica Acta*, *242*, 165–190. https://doi.org/10.1016/j.gca.2018.08.050

Fiege, A., Holtz, F., Behrens, H., Mandeville, C. W., Shimizu, N., Crede, L. S., & Göttlicher, J. (2015). Experimental investigation of the S and S-isotope distribution between H_2O–S±cl fluids and basaltic melts during decompression. *Chemical Geology*, *393-394*, 36–54. https://doi.org/10.1016/j.chemgeo.2014.11.012

Fink, J. H., & Griffiths, R. W. (1998). Morphology, eruption rates, and rheology of lava domes: Insights from laboratory models. *Journal of Geophysical Research*, *103*(B1), 527–545. https://doi.org/10.1029/97JB02838

Fioletov, V. E., McLinden, C. A., Krotkov, N., Li, C., Joiner, J., Theys, N., et al. (2016). A global catalogue of large SO_2 sources and emissions derived from the ozone monitoring instrument. *Atmospheric Chemistry and Physics*, *16*(18), 11,497–11,519. https://doi.org/10.5194/acp-16-11497-2016

Fischer, T. P. (2008). Fluxes of volatiles (H_2O, CO_2, N_2, Cl, F) from arc volcanoes. *Geochemical Journal*, *42*(1), 21–38. https://doi.org/10.2343/geochemj.42.21

Fischer, T. P., Arehart, G. B., Sturchio, N. C., & Williams, S. N. (1996). The relationship between fumarole gas composition and eruptive activity at Galeras volcano, Colombia. *Geology*, *24*(6), 531–534. https://doi.org/10.1130/0091-7613(1996)024<0531:TRBFGC>2.3.CO;2

Ghiorso, M. S., & Gualda, G. A. R. (2015). An H2O-CO2 mixed fluid saturation model compatible with rhyolite-MELTS. *Contributions to Mineralogy and Petrology*, *169*(6). https://doi.org/10.1007/s00410-015-1141-8

Giggenbach, W. F. (1992). Isotopic shifts in waters from geothermal and volcanic systems along convergent plate boundaries and their origin. *Earth and Planetary Science Letters*, *113*(4), 495–510. https://doi.org/10.1016/0012-821X(92)90127-H

Giggenbach, W. F., & Matsuo, S. (1991). Evaluation of results from 2nd and 3rd Iavcei field workshops on volcanic gases, Mt Usu, Japan, and White-Island. *New-Zealand*, *6*(2), 125–141.

Giordano, D., Russell, J. K., & Dingwell, D. B. (2008). Viscosity of magmatic liquids: A model. *Earth and Planetary Science Letters*, *271*(1-4), 123–134. https://doi.org/10.1016/j.epsl.2008.03.038

Gliß, J., Stebel, K., Kylling, A., Dinger, A. S., Sihler, H., & Sudbø, A. (2017). Pyplis—A Python software toolbox for the analysis of SO_2 camera images for emission rate retrievals from point sources. *Geosciences*, *7*(4), 134. https://doi.org/10.3390/geosciences7040134

Gliß, J., Stebel, K., Kylling, A., & Sudbø, A. (2018). Improved optical flow velocity analysis in SO_2 camera images of volcanic plumes—Implications for emission-rate retrievals investigated at Mt Etna, Italy and Guallatiri, Chile. *Atmospheric Measurement Techniques*, *11*(2), 781–801. https://doi.org/10.5194/amt-11-781-2018

Gómez-Vazquez, A., De la Cruz-Reyna, S., & Mendoza-Rosas, A. T. (2016). The ongoing dome emplacement and destruction cyclic process at Popocatépetl volcano, Central Mexico. *Bulletin of Volcanology*, *78*(9), 58. https://doi.org/10.1007/s00445-016-1054-z

Grainger, J. F., & Ring, J. (1962). Anomalous Fraunhofer line profiles. *Nature*, *193*(4817), 762–762. https://doi.org/10.1038/193762a0

Haney, M., Lyons, J. J., Power, J. A., & Roman, D. C. (2019). *Moment tensors of small vulcanian explosions at Mount Cleveland* (pp. V41A–V05A). Alaska: American Geophysical Union, San Fransisco.

Hartley, M. E., Maclennan, J., Edmonds, M., & Thordarson, T. (2014). Reconstructing the deep CO_2 degassing behaviour of large basaltic fissure eruptions. *Earth and Planetary Science Letters*, *393*, 120–131. https://doi.org/10.1016/j.epsl.2014.02.031

Herrick, J. A., Neal, C. A., Cameron, C. E., Dixon, J. P., & McGimsey, R. G. (2014). *2012 volcanic activity in Alaska—Summary of events and response of the Alaska Volcano Observatory*. U.S. Geological Survey Scientific Investigations Report 2014–5160.

Hidalgo, S., Battaglia, J., Arellano, S., Sierra, D., Bernard, B., Parra, R., et al. (2018). Evolution of the 2015 Cotopaxi eruption revealed by combined geochemical and seismic observations. *Geochemistry Geophysics Geosystems*, *19*, 2087–2108. https://doi.org/10.1029/2018GC007514

Hsieh, P. A., & Ingebritsen, S. E. (2019). Groundwater inflow toward a preheated volcanic conduit: Application to the 2018 eruption at Kīlauea volcano, Hawai'i. *Journal of Geophysical Research: Solid Earth*, *124*, 1498–1506. https://doi.org/10.1029/2018JB017133

Iacono-Marziano, G., Morizet, Y., Le Trong, E., & Gaillard, F. (2012). New experimental data and semi-empirical parameterization of H_2O-CO_2 solubility in mafic melts. *Geochimica et Cosmochimica Acta*, *97*, 1–23. https://doi.org/10.1016/j.gca.2012.08.035

Janiszewski, H. A., Wagner, L. S., & Roman, D. C. (2020). Aseismic mid-crustal magma reservoir at Cleveland volcano imaged through novel receiver function analyses. *Scientific Reports*, *10*(1), 1780. https://doi.org/10.1038/s41598-020-58589-0

Johnson, E. A., & Rossman, G. R. (2013). The diffusion behavior of hydrogen in plagioclase feldspar at 800–1000 °C: Implications for re-equilibration of hydroxyl in volcanic phenocrysts. *American Mineralogist*, *98*(10), 1779–1787. https://doi.org/10.2138/am.2013.4521

Johnson, E. R., Wallace, P. J., Cashman, K. V., & Granados, H. D. (2010). Degassing of volatiles (H_2O, CO_2, S, Cl) during ascent, crystallization, and eruption at mafic monogenetic volcanoes in Central Mexico. *Journal of Volcanology and Geothermal Research*, *197*(1–4), 225–238. https://doi.org/10.1016/j.jvolgeores.2010.02.017

Kazahaya, K., Shinohara, H., & Saito, G. (1994). Excessive degassing of Izu-Oshima volcano; magma convection in a conduit. *Bulletin of Volcanology*, *56*(3), 207–216. https://doi.org/10.1007/BF00279605

Kelly, P. J., Kern, C., Roberts, T. J., Lopez, T., Werner, C., & Aiuppa, A. (2013). Rapid chemical evolution of tropospheric volcanic emissions from redoubt volcano, Alaska, based on observations of ozone and halogen-containing gases. *Journal of Volcanology and Geothermal Research*, *259*, 317–333. https://doi.org/10.1016/j.jvolgeores.2012.04.023

Kent, A. J. R., Norman, M. D., Hutcheon, I. D., & Stolper, E. M. (1999). Assimilation of seawater-derived components in an oceanic volcano: Evidence from matrix glasses and glass inclusions from Loihi seamount, Hawaii. *Chemical Geology*, *156*(1-4), 299–319. https://doi.org/10.1016/S0009-2541(98)00188-0

Kern, C., Deutschmann, T., Vogel, L., Wöhrbach, M., Wagner, T., & Platt, U. (2010). Radiative transfer corrections for accurate spectroscopic measurements of volcanic gas emissions. *Bulletin of Volcanology*, *72*(2), 233–247. https://doi.org/10.1007/s00445-009-0313-7

Kern, C., Kick, F., Lübcke, P., Vogel, L., Wöhrbach, M., & Platt, U. (2010). Theoretical description of functionality, applications, and limitations of SO_2 cameras for the remote sensing of volcanic plumes. *Atmospheric Measurement Techniques*, *3*(3), 733–749. https://doi.org/10.5194/amt-3-733-2010

Kern, C., Lübcke, P., Bobrowski, N., Campion, R., Mori, T., Smekens, J.-F., et al. (2015). Intercomparison of SO_2 camera systems for imaging volcanic gas plumes. *Journal of Volcanology and Geothermal Research*, *300*, 22–36. https://doi.org/10.1016/j.jvolgeores.2014.08.026

Kern, C., Masias, P., Apaza, F., Reath, K. A., & Platt, U. (2017). Remote measurement of high preeruptive water vapor emissions at Sabancaya volcano by passive differential optical absorption spectroscopy. *Journal of Geophysical Research: Solid Earth*, *122*, 3540–3564. https://doi.org/10.1002/2017JB014020

Kissling, E., Ellsworth, W., Eberhart-Phillips, D., & Kradolfer, U. (1994). Initial reference models in local earthquake tomography. *Journal of Geophysical Research*, *991*, 19,635–19,646.

Kraus, S. (2006). *DOASIS: A framework design for DOAS*. Aachen: Shaker.

Lesher, C. E., & Spera, F. J. (2015). Chapter 5—Thermodynamic and transport properties of silicate melts and magma. In H. Sigurdsson (Ed.), *The encyclopedia of volcanoes* (Second ed.pp. 113–141). Amsterdam: Academic Press. https://doi.org/10.1016/B978-0-12-385938-9.00005-5

Lienert, B. R., & Havskov, J. (1995). A computer program for locating earthquakes both locally and globally. *Seismological Research Letters*, *66*(5), 26–36. https://doi.org/10.1785/gssrl.66.5.26

Lloyd, A., Plank, T., Ruprecht, P., Hauri, E., & Rose, W. I. (2010). Volatile loss from melt inclusions in clasts of differing sizes. *Contributions to Mineralogy and Petrology*, *165*.

Lloyd, A. S., Plank, T., Ruprecht, P., Hauri, E. H., & Rose, W. (2013). Volatile loss from melt inclusions in pyroclasts of differing sizes. *Contributions to Mineralogy and Petrology*, *165*(1), 129–153. https://doi.org/10.1007/s00410-012-0800-2

López, T., Ushakov, S., Izbekov, P., Tassi, F., Cahill, C., Neill, O., & Werner, C. (2013). Constraints on magma processes, subsurface conditions, and total volatile flux at Bezymianny volcano in 2007–2010 from direct and remote volcanic gas measurements. *Journal of Volcanology and Geothermal Research*, *263*, 92–107. https://doi.org/10.1016/j.jvolgeores.2012.10.015

Lowenstern, J. B. (1995). Applications of silicate-melt inclusions to the study of magmatic volatiles. *Magmas, fluids, and ore deposits*, *23*, 71–99.

Lu, Z., & Dzurisin, D. (2014). *InSAR imaging of Aleutian Volcanoes, InSAR imaging of Aleutian volcanoes: Monitoring a volcanic arc from space* (pp. 87–345). Berlin, Heidelberg: Springer. https://doi.org/10.1007/978-3-642-00348-6_6

Melnik, O., Barmin, A. A., & Sparks, R. S. J. (2005). Dynamics of magma flow inside volcanic conduits with bubble overpressure buildup and gas loss through permeable magma. *Journal of Volcanology and Geothermal Research*, *143*(1-3), 53–68. https://doi.org/10.1016/j.jvolgeores.2004.09.010

Métrich, N., & Wallace, P. J. (2008). Volatile abundances in basaltic magmas and their degassing paths tracked by melt inclusions. *Reviews in Mineralogy and Geochemistry*, *69*(1), 363–402. https://doi.org/10.2138/rmg.2008.69.10

Mironov, N., Portnyagin, M., Botcharnikov, R., Gurenko, A., Hoernle, K., & Holtz, F. (2015). Quantification of the CO_2 budget and H_2O–CO_2 systematics in subduction-zone magmas through the experimental hydration of melt inclusions in olivine at high H_2O pressure. *Earth and Planetary Science Letters*, *425*, 1–11. https://doi.org/10.1016/j.epsl.2015.05.043

Moore, G. (2008). Interpreting H_2O and CO_2 contents in melt inclusions: Constraints from solubility experiments and modeling. *Reviews in Mineralogy and Geochemistry*, *69*(1), 333–362. https://doi.org/10.2138/rmg.2008.69.9

Moore, L., Gazel, E., Tuohy, R., Lloyd, A., Esposito, R., Steele-MacInnis, M., et al. (2015). Bubbles matter: An assessment of the contribution of vapor bubbles to melt inclusion volatile budgets. *American Mineralogist*, *100*(4), 806–823. https://doi.org/10.2138/am-2015-5036

Moretti, R., & Papale, P. (2004). On the oxidation state and volatile behavior in multicomponent gas-melt equilibria. *Chemical Geology*, *213*(1–3), 265–280. https://doi.org/10.1016/j.chemgeo.2004.08.048

Mori, T., & Burton, M. (2006). The SO_2 camera: A simple, fast and cheap method for ground-based imaging of SO_2 in volcanic plumes. *Geophysical Research Letters*, *33*, L24804. https://doi.org/10.1029/2006GL027916

Moussallam, Y., Tamburello, G., Peters, N., Apaza, F., Schipper, C. I., Curtis, A., et al. (2017). Volcanic gas emissions and degassing dynamics at Ubinas and Sabancaya volcanoes; implications for the volatile budget of the central volcanic zone. *Journal of Volcanology and Geothermal Research*, *343*(Supplement C), 181–191.

Neal, C., Izbekov, P. and Nicolaysen, K. (2015). *Preliminary analysis of a postglacial tephra section at Mount Cleveland volcano, Chuginadak Island, Aleutian Arc*, Geological Society of America, Abstracts with Programs.

Neal, C. A., McGimsey, R. G., Dixon, J. P., Cameron, C. E., Nuzhdaev, A. A., & Chibisova, M. (2011). *2008 volcanic activity in Alaska, Kamchatka, and the Kurile Islands: Summary of events and response of the Alaska volcano Observatory*, USGS.

Newman, S., & Lowenstern, J. B. (2002). VolatileCalc: A silicate melt-H_2O-CO_2 solution model written in Visual Basic for Excel. *Computers & Geosciences*, *28*(5), 597–604. https://doi.org/10.1016/S0098-3004(01)00081-4

Ogburn, S. E., Loughlin, S. C., & Calder, E. S. (2015). The association of lava dome growth with major explosive activity (VEI ≥ 4): DomeHaz, a global dataset. *Bulletin of Volcanology*, *77*(5), 40. https://doi.org/10.1007/s00445-015-0919-x

Papale, P., Moretti, R., & Barbato, D. (2006). The compositional dependence of the saturation surface of H_2O + CO_2 fluids in silicate melts. *Chemical Geology*, *229*(1–3), 78–95. https://doi.org/10.1016/j.chemgeo.2006.01.013

Pering, T. D., McGonigle, A. J. S., James, M. R., Tamburello, G., Aiuppa, A., Delle Donne, D., & Ripepe, M. (2016). Conduit dynamics and post explosion degassing on Stromboli: A combined UV camera and numerical modeling treatment. *Geophysical Research Letters*, *43*, 5009–5016. https://doi.org/10.1002/2016GL069001

Platt, U., & Stutz, J. (2008). *Differential absorption spectroscopy, differential optical absorption spectroscopy* (pp. 135–174). Berlin, Heidelberg: Springer.

Power, J. A., Roman, D. C., Lyons, J. J., & Haney, M. M. (2017). Seismic observations of Mount Cleveland, Alaska, a frequently active volcano in the central Aleutian Arc. In: IAVCEI (Editor), IAVCEI 2017 General Assembly, Portland, OR.

Putirka, K. D., Perfit, M., Ryerson, F., & Jackson, M. G. (2007). Ambient and excess mantle temperatures, olivine thermometry, and active vs. passive upwelling. *Chemical Geology*, *241*(3–4), 177–206. https://doi.org/10.1016/j.chemgeo.2007.01.014

Rasmussen, D. J. (2019). *The Aleutian Arc through and through: Subduction dynamics and the generation, storage, and eruption of hydrous magmas*. New York, NY: Columbia University.

Rasmussen, D. J., Kyle, P. R., Wallace, P. J., Sims, K. W. W., Gaetani, G. A., & Phillips, E. H. (2017). Understanding degassing and transport of CO_2-rich Alkalic magmas at Ross Island, Antarctica using olivine-hosted melt inclusions. *Journal of Petrology*, *58*(5), 841–861.

Rasmussen, D. J., Plank, T. A., Wallace, P. J., Newcombe, M. E., & Lowenstern, J. B. (in press). Vapor bubble growth in olivine-hosted melt inclusions. *American Mineralogist*. https://doi.org/10.2138/am-2020-7377

Rasmussen, D. J., Plank, T. A., Roman, D. C., Power, J. A., Bodnar, R. J., & Hauri, E. H. (2018). When does eruption run-up begin? Multidisciplinary insight from the 1999 eruption of Shishaldin volcano. *Earth and Planetary Science Letters*, *486*, 1–14. https://doi.org/10.1016/j.epsl.2018.01.001

Reubi, O., & Blundy, J. (2009). A dearth of intermediate melts at subduction zone volcanoes and the petrogenesis of arc andesites. *Nature*, *461*(7268), 1269–1273. https://doi.org/10.1038/nature08510

Rose, W. I., Palma, J. L., Granados, H. D., & Varley, N. (2013). *Open-vent volcanism and related hazards: Overview*, Special Paper of the Geological Society of America (pp. vii-xiii).

Shinoara, H., Fukui, K., Kazahaya, K., & Saito, G. (2003). In B. de Vivo, & R. J. Bodnar (Eds.), *Degassing process of Miyakejima volcano; implications of gas emission rate and melt inclusion data*. Amsterdam: Elsevier.

Shinohara, H. (2005). A new technique to estimate volcanic gas composition; plume measurements with a portable multi-sensor system. *Journal of Volcanology and Geothermal Research*, *143*(4), 319–333. https://doi.org/10.1016/j.jvolgeores.2004.12.004

Shinohara, H. (2008). Excess degassing from volcanoes and its role on eruptive and intrusive activity. *Reviews of Geophysics*, *46*, RG4005. https://doi.org/10.1029/2007RG000244

Sisson, T., & Layne, G. (1993). H2O in basalt and basaltic andesite glass inclusions from four subduction-related volcanoes. *Earth and Planetary Science Letters*, *117*(3–4), 619–635. https://doi.org/10.1016/0012-821X(93)90107-K

Siswowidjoyo, S., Suryo, I., & Yokoyama, I. (1995). Magma eruption rates of Merapi volcano, Central Java, Indonesia during one century (1890–1992). *Bulletin of Volcanology*, *57*(2), 111–116. https://doi.org/10.1007/BF00301401

Spilliaert, N., Métrich, N., & Allard, P. (2006). S–Cl–F degassing pattern of water-rich alkali basalt: Modelling and relationship with eruption styles on Mount Etna volcano. *Earth and Planetary Science Letters*, *248*(3–4), 772–786. https://doi.org/10.1016/j.epsl.2006.06.031

Steele-Macinnis, M., Esposito, R., & Bodnar, R. J. (2011). Thermodynamic model for the effect of post-entrapment crystallization on the H_2O–CO_2 systematics of vapor-saturated, silicate melt inclusions. *Journal of Petrology*, *52*(12), 2461–2482. https://doi.org/10.1093/petrology/egr052

Symonds, R. B., Rose, W. I., Bluth, G. S., & Gerlach, T. M. (1994). Volcanic gas studies: Methods, results, and applications. In M. R. Carroll, & J. R. Holloway (Eds.), *Volatiles in magmas. Mineralogical Society of America* (pp. 1–60). Washington, DC: Mineralogical Society of America.

Symonds, R. B., Rose, W. I., Gerlach, T. M., Briggs, P. H., & Harmon, R. S. (1990). Evaluation of gases, condensates, and SO_2 emissions from Augustine volcano, Alaska: The degassing of a Cl-rich volcanic system. *Bulletin of Volcanology*, *52*(5), 355–374. https://doi.org/10.1007/BF00302048

Tamburello, G., Aiuppa, A., McGonigle, A. J. S., Allard, P., Cannata, A., Giudice, G., et al. (2013). Periodic volcanic degassing behavior: The Mount Etna example. *Geophysical Research Letters*, *40*, 4818–4822. https://doi.org/10.1002/grl.50924

Vandaele, A. C., Hermans, C., & Fally, S. (2009). Fourier transform measurements of SO_2 absorption cross sections: II.: Temperature dependence in the 29000–44000cm−1 (227–345nm) region. *Journal of Quantitative Spectroscopy and Radiative Transfer*, *110*(18), 2115–2126. https://doi.org/10.1016/j.jqsrt.2009.05.006

Wade, J. A., Plank, T., Stern, R. J., Tollstrup, D. L., Gill, J. B., O'Leary, J. C., et al. (2005). The May 2003 eruption of Anatahan volcano, Mariana Islands: Geochemical evolution of a silicic island-arc volcano. *Journal of Volcanology and Geothermal Research*, *146*(1–3), 139–170. https://doi.org/10.1016/j.jvolgeores.2004.11.035

Wang, T., Poland, M. P., & Lu, Z. (2015). Dome growth at Mount Cleveland, Aleutian arc, quantified by time series TerraSAR-X imagery. *Geophysical Research Letters*, *42*(24), 10,614–10,621. https://doi.org/10.1002/2015GL066784

Werner, C., Fischer, T. P., Aiuppa, A., Edmonds, M., Cardellini, C., Carn, S., et al. (2019). Carbon dioxide emissions from subaerial volcanic regions: Two decades in review. In B. N. Orcutt, I. Daniel, & R. Dasgupta (Eds.), *Deep Carbon: Past to Present* (pp. 188–236). Cambridge: Cambridge University Press. https://doi.org/10.1017/9781108677950.008

Werner, C., Kelly, P. J., Doukas, M., Lopez, T., Pfeffer, M., McGimsey, R., & Neal, C. (2013). Degassing of CO_2, SO_2, and H_2S associated with the 2009 eruption of Redoubt volcano, Alaska. *Journal of Volcanology and Geothermal Research*, *259*, 270–284. https://doi.org/10.1016/j.jvolgeores.2012.04.012

Werner, C., Kern, C., Coppola, D., Lyons, J. J., Kelly, P. J., Wallace, K. L., et al. (2017). Magmatic degassing, lava dome extrusion, and explosions from Mount Cleveland volcano, Alaska, 2011–2015: Insight into the continuous nature of volcanic activity over multi-year timescales. *Journal of Volcanology and Geothermal Research*, *337*, 98–110. https://doi.org/10.1016/j.jvolgeores.2017.03.001

Werner, C. A., Doukas, M. P., & Kelly, P. J. (2011). Gas emissions from failed and actual eruptions from cook inlet volcanoes, Alaska, 1989–2006. *Bulletin of Volcanology*, *73*(2), 155–173. https://doi.org/10.1007/s00445-011-0453-4

Witham, F., Blundy, J., Kohn, S. C., Lesne, P., Dixon, J., Churakov, S. V., & Botcharnikov, R. (2012). SolEx: A model for mixed COHSCl-volatile solubilities and exsolved gas compositions in basalt. *Computers & Geosciences*, *45*, 87–97. https://doi.org/10.1016/j.cageo.2011.09.021

Witter, J., Kress, V., & Newhall, C. (2005). Volcán Popocatépetl, Mexico. Petrology, magma mixing, and immediate sources of volatiles for the 1994–present eruption. *Journal of Petrology*, *46*(11), 2337–2366. https://doi.org/10.1093/petrology/egi058

Zhang, Y., Xu, Z., Zhu, M., & Wang, H. (2007). Silicate melt properties and volcanic eruptions. *Reviews of Geophysics*, *45*, RG4004.

Zimmer, M. M., Plank, T., Hauri, E. H., Yogodzinski, G. M., Stelling, P., Larsen, J., et al. (2010). The role of water in generating the Calc-alkaline trend: New volatile data for Aleutian magmas and a new Tholeiitic index. *Journal of Petrology*, *51*(12), 2411–2444. https://doi.org/10.1093/petrology/egq062